

SuperQuadricOcc: Real-Time Self-Supervised Semantic Occupancy Estimation with Superquadric Volume Rendering

Seamie Hayes^{1,2}, Alexandre Boulch³, Andrei Bursuc³, Reenu Mohandas¹, Ganesh Sistu¹, Tim Brophy¹, Ciarán Eising^{1,2}

¹ Data Driven Computer Engineering (D²iCE) Research Centre, University of Limerick, V94 T9PX Ireland.

² Taighde Éireann – Research Ireland, University of Limerick, V94 T9PX Ireland
³ valeo.ai, 75008 Paris, France

Abstract. Self-supervision for semantic occupancy estimation is appealing as it removes the labour-intensive manual annotation, thus allowing one to scale to larger autonomous driving datasets. Superquadrics offer an expressive shape family very suitable for this task, yet their deployment in a self-supervised setting has been hindered by the lack of efficient rendering methods to bridge the 3D scene representation and 2D training pseudo-labels. To address this, we introduce SuperQuadricOcc, the first self-supervised occupancy model to leverage superquadrics for scene representation. To overcome the rendering limitation, we propose a real-time volume renderer that preserves the fidelity of the superquadric shape during rendering. It relies on spatial superquadric-voxel indexing, restricting each ray sample to query only nearby superquadrics, thereby greatly reducing memory usage and computational cost. Using drastically fewer primitives than previous Gaussian-based methods, SuperQuadricOcc achieves state-of-the-art performance on the Occ3D-nuScenes dataset, while running at real-time inference speeds with substantially reduced memory footprint. [SuperQuadricOcc GitHub](#)

Keywords: SuperQuadric · Occupancy · Volume Rendering

1 Introduction

Ensuring safety for autonomous perception requires complex and accurate scene modelling. Current research primarily focuses on semantic occupancy estimation, which represents the world as a discretised voxel grid. This reduces limitations in the previous spatial understanding methods, such as the rigid cuboid prediction space of 3D object detection and the lack of verticality in Bird’s Eye View (BEV).

In a supervised setting, where the predictions and the ground truth space are aligned [28], semantic occupancy estimation has evolved from dense voxel-based formats to more efficient Gaussian representations, and most recently, to superquadrics [61, 66]. The latter’s reduced-memory footprint and high inference speed make them highly attractive for real-time autonomous perception. In contrast, self-supervised methods do not rely on comprehensive ground-truth annotations, significantly reducing the need for costly manual labelling and improving

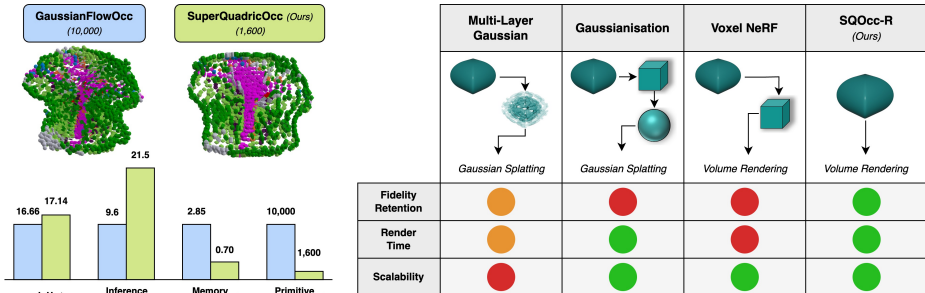


Fig. 1: SuperQuadricOcc and SuperQuadricOcc-Render. *SQOcc* achieves higher mIoU, faster inference, and lower memory consumption with much fewer primitives compared to GaussianFlowOcc. *SQOcc-R*'s direct rendering of primitives preserves geometric accuracy in contrast to other rendering methods (Gaussian or voxels).

scalability for large datasets and models. However, supervision is now derived from 2D pseudo-labels, and hence rendering techniques are required to bridge 3D scene representations with 2D supervision space [7]. While voxel-based [62] and Gaussian-based methods [29] directly benefit rendering techniques such as volume rendering and 3D Gaussian Splatting (3DGS) [32], superquadrics lack a native rasterisation method.

We address these challenges by introducing SuperQuadricOcc (SQOcc for short) and SuperQuadricOcc-Render (SQOcc-R for short). To our knowledge, the former is the first self-supervised model based on superquadrics for semantic occupancy estimation. The latter is a real-time CUDA-accelerated superquadric volume renderer specifically designed for superquadrics. It relies on spatial indexing to establish a superquadric-voxel correspondence which restricts the influence of superquadrics to nearby regions, similar to the efficiency of screen-space rasterisation in 3DGS [32]. As a result, each ray sample attends only to superquadrics with a significant contribution, substantially reducing computational overhead and enabling the rendering of large numbers of superquadrics.

SQOcc achieves state-of-the-art results on the Occ3D-nuScenes dataset [48] across performance metrics, memory efficiency, and achieves real-time inference, benefiting from the compact representation of superquadrics. Our rendering method demonstrates superior performance in quality metrics due to fidelity retention and significantly reduces memory consumption compared to challengers. Furthermore, it proves scalability with increasing superquadric count. As illustrated in Figure 1, our major contributions are:

1. **Scene Representation.** We introduce SQOcc, the first self-supervised semantic occupancy model to represent scenes using superquadrics.
2. **View Renderer.** We develop SQOcc-R, a superquadric volume renderer that utilises spatial indexing to efficiently manage thousands of primitives and achieve 58 FPS real-time inference for six nuScenes cameras.

3. **Performances.** We obtain state-of-the-art performance on Occ3D-nuScenes, achieving 17.14 mIoU and 17.26 RayIoU. Furthermore, our model reaches real-time inference at 21.5 FPS with a memory footprint of 0.70 GB.

2 Related Work

Semantic Occupancy Estimation. The gain of interest for semantic occupancy estimation for autonomous vehicle perception has been enabled by large-scale occupancy datasets [48, 49, 55, 58], built upon benchmarks such as nuScenes [8] and SemanticKITTI [6]. Scene representations have rapidly evolved from strictly voxel-based methods [22, 41, 51, 67], to Gaussian-based approaches [25, 28, 65, 68], and more recently to superquadric-based representations [61, 66]. This progression is largely driven by the advantages of sparse scene representations, including reduced memory consumption and faster inference times.

Self-supervision for semantic occupancy. Beyond representation choice, supervision strategy forms another key axis of development. Fully supervised methods initially dominated the field [27, 37, 38]. However, more recently, fully self-supervised methods have seen a rise in usage, particularly due to the lack of need for manual annotation, greatly reducing labour costs and increasing scalability. Such methods rely solely on 2D pseudo-labels generated by Vision–Language Models (VLMs) [4, 44] and Visual Foundation Models (VFMs) [4, 24, 45, 64] for supervision. Voxel-based approaches [26, 62] suffer from high computational costs and slow inference, driven by large convolutional operations and inefficient supervision via voxel-wise volume rendering. Gaussian-based methods subsequently emerged but are hindered at inference by a reliance on large Vision Foundation Models (VFMs) [29, 63] or high primitive counts [7, 63], both of which compromise real-time deployment and memory efficiency. In contrast, SQOcc achieves real-time inference and a reduced memory footprint—all while improving performance metrics without the need for inference-time VFMs.

Novel View Synthesis aims to render a scene or object from viewpoints different from those of the images used to extract priors. Currently, the main approaches are Neural Radiance Fields (NeRF) and 3DGS [32]. The former uses an implicit scene representation and volume rendering, while the latter employs Gaussian-based scene representation and screen-space rasterisation. Both approaches have been widely applied across many domains [10, 16, 59] ranging from medical imaging [5, 11, 40, 52, 56] and robotics [13, 21, 35, 39, 46] to 3D reconstruction [2, 23, 31, 43, 54].

For 3D object reconstruction specifically, PartGS [17] and GaussianBlock [30] draw inspiration from work that places Gaussians on mesh surfaces [18, 50], extending this idea by positioning Gaussians on superquadric surfaces to act as a rendering proxy. OccNeRF [62] adopts a NeRF-style voxel-volume rendering formulation, while GaussianOcc [14] introduces a voxel-to-Gaussian module for 3DGS. We adapt these methods as baselines for our rendering approach.

Finally, ISCO [1] reconstructs single objects using superquadrics and NeRF-style volume rendering for supervision against ground-truth 2D object silhou-

ettes. However, it is not suitable for modelling the complexity of outdoor scenes as it is limited to ten primitives maximum, naively querying every superquadric for every ray sample. In contrast, our approach is capable of handling thousands of superquadric primitives through an efficient spatial indexing strategy, enabling real-time rendering with minimal fidelity loss.

3 Methodology

3.1 SuperQuadratics

We represent the scene using a set of N superquadric primitives, $\mathcal{S} = \{S_i\}_{i=1}^N$, where each primitive is defined as: $S_i = \{\mathbf{m}_i, \mathbf{s}_i, \mathbf{r}_i, \varepsilon_i, \sigma_i, \mathbf{c}_i\}$. Where \mathbf{m} is the center, $\mathbf{s} = (s_x, s_y, s_z)$ the scale along the three principal axes, $\mathbf{r} \in \mathbb{R}^4$ a quaternion rotation, and $\varepsilon = (\varepsilon_1, \varepsilon_2)$ controls the squareness and roundness of the shape. $\sigma \in \mathbb{R}$ is the density, and $\mathbf{c} \in \mathbb{R}^C$ encodes semantic information over C classes. The implicit surface equation of a canonical superquadric [3] is:

$$f(\mathbf{x}) = \left(\left(\frac{x}{s_x} \right)^{\frac{2}{\varepsilon_2}} + \left(\frac{y}{s_y} \right)^{\frac{2}{\varepsilon_2}} \right)^{\frac{\varepsilon_2}{\varepsilon_1}} + \left(\frac{z}{s_z} \right)^{\frac{2}{\varepsilon_1}} \quad (1)$$

where $\mathbf{x} = (x, y, z)$ is expressed in the canonical frame. To model occupancy probability, Zuo *et al.* [66] proposed an exponential decay formulation analogous to that of a Gaussian distribution. The occupancy probability of superquadric S at a 3D point \mathbf{x} is defined as:

$$p_o(\mathbf{x}, S) = \sigma \exp(-f(\mathbf{x}_S)), \quad \mathbf{x}_S = R(\mathbf{x} - \mathbf{m}) \quad (2)$$

where \mathbf{x}_S is \mathbf{x} transformed into the canonical superquadric coordinate system, and R is the rotation matrix corresponding to quaternion \mathbf{r} . In this exponential formulation, the ε parameters now also control the rate of decay. This formulation is fully differentiable, enabling efficient gradient-based optimisation for our render pipeline. We adopt this formulation both for rendering and voxelization.

3.2 Model Framework

The architecture of SuperQuadricOcc is based on GaussianFlowOcc [7], adapted for a superquadric scene representation. It is illustrated in Figure 2. We utilise a ResNet-50 backbone which extracts features, \hat{I} , which along with superquadric primitive features $S_F \in \mathbb{R}^{N \times C}$ and means $S_M \in \mathbb{R}^{N \times 3}$, are passed to the Transformer network, which iteratively refines S_F and S_M in B blocks before predicting the final properties of the superquadric primitive set \mathcal{S} .

The Transformer network uses temporal attention $\text{TA}(S_F^T, S_F^{T-1})$ against previous features for efficient temporal propagation. Following this, self-attention is employed $\text{SA}(S_F^T, S_F^T)$ for spatial interaction, and then deformable attention $\text{DA}(\hat{I}, S_F)$ is performed for enriching with image features. All attention mechanisms use induced attention [33], with positional encoding of S_M .

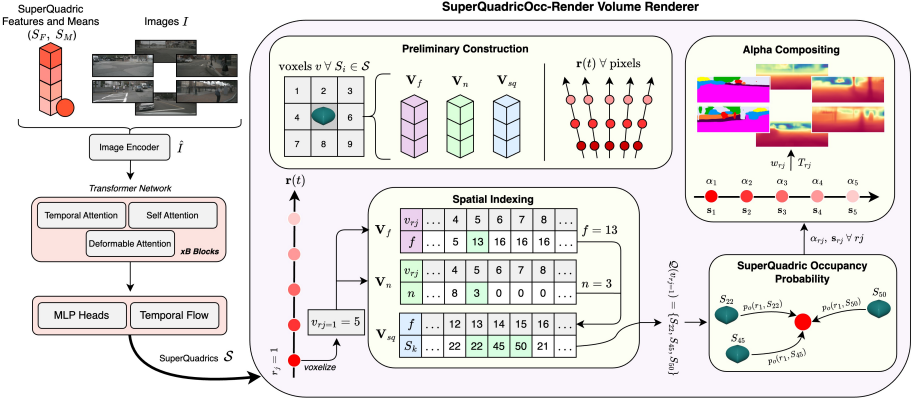


Fig. 2: SuperQuadricOcc Model Architecture: The transformer network refines superquadric means S_M and features S_F , which are eventually transformed into full primitives for rendering. In SuperQuadricOcc-Render, following preliminary construction, we iterate over each ray sample r_j , and query the spatial indexing tensors V_{sq}, V_n, V_f to attain the list of superquadratics $\mathcal{Q}(v_{r_j})$. We calculate the ray sample values, α_{r_j}, s_{r_j} , and perform alpha compositing for the final semantic \hat{S} and depth \hat{D} renders. During evaluation, superquadratics S are voxelized.

After refinement, each superquadric property $\{\mathbf{s}, \mathbf{r}, \varepsilon, \sigma, \mathbf{c}\}$, excluding mean, is attained by passing S_F to individual lightweight MLPs. Finally, a temporal flow module is employed, which propagates S_M for each frame in the temporal horizon ($t \in [-T, T]$). This is achieved by passing learnable tokens $\Psi \in \mathbb{R}^{2T \times D}$ and S_F to an MLP to get an offset vector $\mathbf{v}(t)$ for each t in the horizon:

$$\mathbf{v}(t) = \text{MLP}(S_F \oplus \Psi(t)) \quad (3)$$

These offsets are added to S_M . Following this, the superquadric sets S in the temporal horizon are passed to the SuperQuadricOcc-Render Volume Renderer.

3.3 SuperQuadricOcc-Render Volume Renderer

In this section, we describe our proposed superquadric rendering method, which leverages CUDA for real-time performance. SuperQuadricOcc-Render directly queries the superquadric occupancy probability equation, resulting in minimal fidelity loss compared to alternative rendering strategies. We first outline the spatial indexing and ray construction, followed by a detailed description of the forward and backward passes. An illustration is provided in Figure 2.

Preliminary Construction: To reduce computation while preserving rendering fidelity, we restrict each ray sample to interact only with superquadratics within a localised neighbourhood. We parameterise the scene as a voxel grid with bounds

and resolution matching those defined in [subsection 4.1](#). For each $S_i \in \mathcal{S}$, we construct a tensor that stores the voxel indices (v), within a cubic neighbourhood \mathcal{N}_v . This tensor is denoted as $\mathbf{V}_c \in \mathbb{Z}^{N \times (2\mathcal{N}_v + 1)^3 \times 3}$.

We then apply hashing to convert \mathbf{V}_c into three spatial indexing tensors for efficient mapping from all v in the entire voxel grid to superquadric indices, S_k :

1. \mathbf{V}_{sq} : Stores the superquadric index $S_k \in \mathcal{N}_v$ for all voxel indices v .
2. \mathbf{V}_f : Given v , this tensor provides the starting index offset, f in \mathbf{V}_{sq} from which to retrieve the first S_k .
3. \mathbf{V}_n : Queried after \mathbf{V}_f . It specifies the number of entries, n , in \mathbf{V}_{sq} corresponding to v , indicating how many superquadrics influence v .

We then utilise S_k to obtain the relevant superquadric parameters. Subsequently, we construct ray samples following standard volume rendering procedures. For each pixel ray $\mathbf{r}(t) = \mathbf{o} + t\mathbf{d}$, we sample L uniformly spaced points $\mathbf{x}_{rj} = \mathbf{o} + t_{rj}\mathbf{d}$ along the unit direction \mathbf{d} in 3D space, where t_{rj} is uniformly sampled within the interval $[t_{\text{near}}, t_{\text{far}}]$ and represents the distance from the camera center along \mathbf{r} . Both the forward and backward passes are implemented in CUDA, with 256 rays per block.

Forward Pass: For each ray \mathbf{r} , we traverse the ray samples r_j in a front-to-back manner. We first determine voxel index v_{rj} and query the tensors \mathbf{V}_f and \mathbf{V}_n to retrieve n and f . We then use these to query \mathbf{V}_{sq} to obtain $\mathcal{Q}(v_{rj})$, which contains all S_k in the neighbourhood \mathcal{N}_v . All r_j outside voxel bounds, as well as those for which $\mathbf{V}_n = 0$, are skipped to avoid unnecessary computation.

Next, for each $S_k \in \mathcal{Q}(v_{rj})$ transform r_j into the local coordinate frame of S_k , and compute the occupancy probability $p_o(r_j, S_k)$ according to Equation (2). The probabilities for each S_k are summed to obtain the alpha value, α_{rj} , and the semantic vector \mathbf{s}_{rj} for r_j :

$$\alpha_{rj} = \sum_{S_k \in \mathcal{Q}(v_{rj})} p_o(r_j, S_k), \quad \mathbf{s}_{rj} = \sum_{S_k \in \mathcal{Q}(v_{rj})} p_o(r_j, S_k) \mathbf{c}_{S_k} \quad (4)$$

where \mathbf{c}_{S_k} represents the semantic logits of S_k . After processing every ray sample in \mathbf{r} , the transmittance and corresponding weighting term are computed using front-to-back alpha-compositing to account for occlusion effects:

$$w_{rj} = T_{rj} \alpha_{rj}, \quad T_{rj} = \prod_{\ell=1}^{j-1} (1 - \alpha_{r\ell}) \quad (5)$$

Given t_{rj} , the ray sample distance along the viewing direction, the final depth and semantic output for each ray (pixel) are then given by:

$$\hat{D}_p = \sum_{j=1}^L w_{rj} t_{rj}, \quad \hat{S}_p = \sum_{j=1}^L w_{rj} \mathbf{s}_{rj} \quad (6)$$

Backward Pass: For the backward pass, we divide the procedure into three separate stages that facilitate backpropagation of gradients to the superquadric parameters.

Process 1: First, we recompute the forward pass for \mathbf{r} , storing intermediate tensors required for gradient propagation. Specifically, we store the transmittance T , alpha α , and the inner product between the semantic gradient and the per-sample semantics, $\langle \nabla_{\hat{\mathbf{s}}_r} \mathcal{L}, \mathbf{s}_{rj} \rangle$, which captures the gradient contribution from the semantic map. We recompute these values rather than reusing them from the initial forward pass to reduce memory consumption.

Process 2: Given the upstream gradient with respect to the rendered depth, $\frac{\partial \mathcal{L}}{\partial D_r}$, together with the semantic inner-product term from *Process 1*, we compute the gradient with respect to the rendering weight, $\frac{\partial \mathcal{L}}{\partial w_{rj}}$. Using the recomputed quantities from *Process 1*, we analytically backpropagate through the front-to-back alpha compositing Equations (5) to obtain the gradient with respect to each sample opacity, $\frac{\partial \mathcal{L}}{\partial \alpha_{rj}}$. These opacity gradients are subsequently used in *Process 3* to accumulate gradients for the corresponding superquadric parameters.

Process 3: After computing $\frac{\partial \mathcal{L}}{\partial \alpha_{rj}}$, we propagate this gradient to the superquadric parameters $\{\mathbf{m}, \mathbf{s}, \mathbf{r}, \varepsilon, \sigma, \mathbf{c}\}$. From Equation (4), the gradient with respect to each occupancy probability is given by

$$\frac{\partial \mathcal{L}}{\partial p_o(r_j, S_k)} = \frac{\partial \mathcal{L}}{\partial \alpha_{rj}} \quad (7)$$

Using the superquadric occupancy probability formulation in Equation (2), we apply the chain rule to compute gradients for each parameter of the superquadric. Gradients are accumulated over all rays and samples that interact with a particular superquadric primitive.

3.4 SuperQuadric Voxelisation

To enable direct comparison with previous state-of-the-art methods, we develop a superquadric voxelization module for evaluation. We extend the Gaussian voxelization strategy of Boeder et al. [7] to superquadric primitives. We iterate over each voxel v with centre \mathbf{p} , summing the contributions from all superquadrics S within a cubic neighbourhood of \mathcal{N}_v . Following previous works [7], we set $\mathcal{N}_v = 5$. For each $S_i \in \mathcal{N}_v$, transform v into the local frame of S_i to get $\mathbf{p}_{\mathbf{s}_i}$, and sum the occupancy probability to obtain a density and semantic voxel:

$$v_d(\mathbf{p}) = \sum_{S_i \in \mathcal{N}_v} \exp(-f_i(\mathbf{p}_{\mathbf{s}_i})) \sigma_i \quad v_s(\mathbf{p}) = \sum_{S_i \in \mathcal{N}_v} \exp(-f_i(\mathbf{p}_{\mathbf{s}_i})) \mathbf{c}_i \quad (8)$$

Voxels below a defined threshold τ in v_d are assigned as free in v_s to obtain the final prediction. We assign $\tau = 0.05$ through empirical tuning.

4 Experiments

4.1 Datasets and Metrics

For training, we utilise 2D pseudo-semantic labels [45] and depth labels [24] provided by GaussianFlowOcc [7]. To evaluate occupancy estimation, we use the Occ3D-nuScenes [48] and OpenOccv2 [49] datasets, both built upon the nuScenes dataset [8]. These datasets provide dense occupancy annotations spanning $[-40\text{m}, 40\text{m}]$ along the X and Y axes and $[-1\text{m}, 5.4\text{m}]$ along the Z axis, with a voxel resolution of 0.4m^3 , defined in the ego-vehicle coordinate frame. Evaluation is conducted using the Intersection over Union (IoU), mean Intersection over Union (mIoU), and RayIoU metrics.

For depth estimation, we retain the same perception range as occupancy estimation for consistency. Ground-truth depth is obtained from nuScenes LiDAR data projected into the camera frame, sourced from GaussianOcc [14]. The depth values are clamped to the range $[0.1\text{m}, 80\text{m}]$ to ensure consistency with prior work. Evaluation follows standard depth metrics reported in the literature, Abs Rel, Sq Rel, RMSE, RMSE log, and threshold accuracy metrics (δ).

4.2 Implementation Details

We train our model following the configuration of GaussianFlowOcc [7]. We employ $N = 1600$ superquadrics and a ResNet-50 backbone [20] pretrained on ImageNet [12] with an input image resolution of 256×704 . The Gaussian Transformer network consists of three sequential blocks, with the induced attention module using 500 inducing points. The temporal flow module operates over a temporal horizon of $T = 6$. For SuperQuadricOcc-Render, we use a neighbourhood size of $N_v = 5$, $L = 100$ ray samples, and a sampling range of $[t_{\text{near}}, t_{\text{far}}] = [0.1, 40.0]$, without early ray termination. All methods are trained for 18 epochs with a batch size of 1 on NVIDIA GPUs. For fair comparison, we report memory usage, model inference time, and rendering time with $1 \times \text{A100}$.

4.3 Main Results

3D Occupancy: SuperQuadricOcc demonstrates improved performance compared to existing occupancy approaches in Table 1, achieving 17.1 mIoU, corresponding to a 2.4% increase over prior work [63], without employing foundation models at inference time. In addition, our model requires substantially less memory, using only 0.7 GB, which represents a 92.9% reduction compared to TT-Occ [63], primarily due to the reduction in primitive count from 2M+ Gaussians to 1,600 superquadrics. Furthermore, our approach achieves real-time inference at 21.5 FPS, enabled by the compact superquadric representation.

In Table 2, our model outperforms all competing methods across both datasets for RayIoU. On the Occ3D dataset [48], we surpass the next best model, GaussianFlowOcc [7], by 1.1 points, indicating stronger scene completion capability.

Table 1: State-of-the-art model comparison on Occ3D-nuScenes [48]: Rep. denotes the method of scene representation: Gauss - Gaussian; Quad - SuperQuadric. Mem. denotes the maximum memory (GB) during inference (rendering pipeline not included). All models are self-supervised. The best-performer is highlighted in **bold**.

Method	Rep.	Mem.	FPS	IoU		barrier	bicycle	bus	car	const. veh.	motorcycle	pedestrian	traffic cone	trailer	truck	drive. surf.	sidewalk	terrain	mammade	vegetation
				mIoU	rIoU	0.5	1.0	1.5	2.0	2.5	3.0	3.5	4.0	4.5	5.0	5.5	6.0	6.5	7.0	7.5
DistillNeRF [53]	Voxel	-	2.8	29.1	10.1	1.4	2.1	10.2	10.1	2.6	2.0	5.5	4.6	1.4	7.9	43.0	16.9	15.0	14.1	15.1
SelfOcc [26]	Voxel	3.00	7.4	45.0	10.5	0.2	0.7	5.5	12.5	0.0	0.8	2.1	0.0	0.0	8.3	55.5	26.3	26.5	14.2	5.6
OccNeRF [62]	Voxel	12.68	5.4	46.4	10.8	0.8	0.8	5.1	12.5	3.5	0.2	3.1	1.8	0.5	3.9	52.6	20.8	24.8	18.5	13.2
GaussianOcc [14]	Voxel	11.81	5.4	42.9	11.3	1.8	5.8	14.6	13.6	1.3	2.8	8.0	9.8	0.6	9.6	44.6	20.1	17.6	8.6	10.3
GaussTR [29]	Gauss	1.97	0.3	44.5	13.8	6.5	8.5	21.8	24.3	6.3	15.5	7.9	1.9	6.1	17.2	37.0	17.2	7.2	21.2	10.0
EasyOcc [19]	Voxel	-	5.4	38.9	15.7	1.9	6.7	15.1	21.7	2.7	8.1	15.3	11.1	1.4	12.8	55.8	27.9	22.1	16.1	17.3
GaussianFlowOcc [7]	Gauss	2.85	9.6	40.5	16.7	6.7	9.2	17.5	16.5	4.0	11.9	8.8	9.7	0.6	12.3	49.3	30.8	34.6	17.4	20.8
TT-Occ [63]	Gauss	9.90	0.7	-	16.7	21.5	10.5	10.7	14.7	11.9	12.3	9.7	12.2	4.4	7.9	48.3	23.7	28.3	14.1	20.2
SQOcc (Ours)	Quad	0.70	21.5	43.5	17.1	7.0	8.3	16.6	14.8	3.4	9.1	8.0	8.8	1.1	12.0	64.7	31.4	34.3	16.6	21.0

On the OpenOccv2 dataset [49], the improvement is 1.6 points, further highlighting the effectiveness of the superquadric scene representation and SuperQuadric-Occ-Render rendering capabilities. Furthermore, TT-Occ performs poorly in RayIoU compared to its performance for mIoU, showing the importance of evaluation on multiple metrics. Additionally, our method achieves superior performance across all evaluated RayIoU distance thresholds.

Table 2: Models evaluated on the RayIoU metric: All models are self-supervised. The best-performer is highlighted in **bold**.

Dataset	Method	Rep.	RayIoU	RayIoU@1	RayIoU@2	RayIoU@4
Occ3D [48]	SelfOcc [26]	Voxel	9.6	6.7	9.6	12.5
	OccNeRF [62]	Voxel	10.4	6.9	10.3	14.1
	GaussianOcc [14]	Voxel	11.9	8.7	11.9	15.0
	TT-Occ [63]	Gauss	13.4	10.0	12.9	15.7
	GaussianFlowOcc [7]	Gauss	16.2	11.2	16.2	21.2
	SQOcc (Ours)	Quad	17.3	11.9	17.3	22.56
OpenOccv2 [49]	SelfOcc [26]	Voxel	9.1	5.8	9.1	12.3
	OccNeRF [62]	Voxel	11.4	7.9	11.3	15.0
	GaussianOcc [14]	Voxel	11.7	8.5	11.8	14.8
	GaussianFlowOcc [7]	Gauss	17.1	12.1	17.2	21.9
	SQOcc (Ours)	Quad	18.7	13.4	18.9	23.9

4.4 Rendering method study

To benchmark our proposed SuperQuadricOcc-Render approach, we compare it with alternative rendering methods. For Gaussianisation and Voxel NeRF rendering, we first voxelize the superquadric set \mathcal{S} according to Equation (8), with voxel bounds and resolution specified in subsection 4.1, producing a density voxel grid \mathbf{V}_d and a semantic voxel grid \mathbf{V}_s .

Baselines

Multi-Layer Gaussian Approximation (MLGA): To appropriately model the superquadric occupancy distribution as Gaussian, we extended upon previous works [17, 30]. Given a canonical superquadric $S = (\mathbf{s}, \varepsilon_1, \varepsilon_2)$, we augment its scale parameters with n positive scalars $P = \{p_1, p_2, \dots, p_n\} \subset \mathbb{R}^+$ to define a scaled family of superquadrics: $S_P = \{(p \mathbf{s}, \varepsilon_1, \varepsilon_2) \mid p \in P\}$.

For each $S_p \in S_P$, a tessellated unit icosphere is constructed. Each vertex on the icosphere, defined by spherical coordinates (η, ω) , is mapped to the superquadric surface through signed powers of trigonometric functions, controlled by ε . Then, for each mapped vertex, we place a 3D Gaussian at the centre, for which the scales s_x and s_y provide sufficient coverage.

For a Gaussian G_p with center \mathbf{x}_p sampled on superquadric S_p , we define a corresponding Gaussian \mathbf{x}_{p+1} on S_{p+1} at the same angular coordinates (η, ω) . For G_p , we define the scale s_z and the opacity σ :

$$s_z = \frac{1}{2} \|\mathbf{x}_{p+1}(\eta, \omega) - \mathbf{x}_p(\eta, \omega)\|, \quad \sigma = \sigma_{S_p} \cdot e^{f(\mathbf{m})}.$$

The scale s_z enables each Gaussian to decay gradually along its normal direction, thereby better approximating the superquadric occupancy probability. For Gaussian opacity σ , we deviate from prior formulations, which assign the opacity of each Gaussian to that of the parent superquadric (σ_{S_p}). In our formulation, \mathbf{m} is the Gaussian mean. This scaling aligns the Gaussian occupancy with that of the superquadric, ensuring that the occupancy evaluated at the Gaussian’s centre exactly matches the corresponding value when evaluated in the superquadric distribution. Gaussians are subsequently rendered using 3DGS.

Gaussianisation: For this method, we follow the strategy adopted in prior state-of-the-art work [9, 14]. A spherical Gaussian primitive is instantiated for each voxel in the scene as $(\mathbf{m}, \mathbf{s}, \sigma, \mathbf{c})$ with: the mean \mathbf{m} at voxel center, the scale hyperparameter \mathbf{s} constant across all axes, the opacity σ with value from \mathbf{V}_d , the semantics \mathbf{c} : value from \mathbf{V}_s . Gaussians are subsequently rendered using 3DGS.

Voxel NeRF: We adopt the approach introduced in OccNeRF [62] for volumetric rendering of voxel grids, using the render Equation (6). In this formulation, alpha $\alpha_{r,j}$ and semantic feature $\mathbf{s}_{r,j}$ are obtained via trilinear interpolation of the voxel grids \mathbf{V}_d and \mathbf{V}_s , respectively.

Implementation details for baselines. For MLGA, we use an 80-faced icosahedron, $S_{n=9}$ where $P = [0.5, 0.6, 0.75, 0.9, 1.05, 1.2, 1.6, 2.0, 2.5]$. Due to limitations of this strategy, particularly in retaining fidelity across multiple views, we omit the temporal module during training as it leads to severely degraded results. For Gaussianisation, we set the Gaussian scale to 0.15. For Voxel NeRF, we use $L=75$ ray samples with the same ray sampling range as SQOcc-R.

For depth evaluation render at resolution 396×704 , and use bilinear interpolation to interpolate to the nuScenes [8] image resolution of 900×1600 in line with previous methods [7].

Table 3: Comparison of SuperQuadric rendering methods: The best-performer is highlighted in **bold**. All models are self-supervised.

Method	IoU		RayIoU		Memory (GB)		Render Time (ms)
	mIoU	IoU	Occ3D [48]	OpenOccv2 [49]	Training	Inference	
MLGA	33.7	12.7	10.9	12.5	-	1.35	44.0
Gaussianisation	43.7	17.0	14.5	15.6	6.2	0.8	13.9
Voxel NeRF	42.9	17.1	16.6	17.7	69.4	11.1	102.4
SQOcc-R (Ours)	43.5	17.1	17.3	18.7	13.7	2.8	17.2

(a) Semantic Occupancy. Memory refers to the maximum memory usage across training and inference (rendering pipeline included during inference). Render time is the average time to render the entire validation data.

Method	Rep.	Abs		RMSE		δ		
		Rel ↓	Sq Rel ↓	↓	log ↓	<1.25↑	<1.25 ² ↑	<1.25 ³ ↑
SurroundDepth [57]	Image	0.280	4.401	7.467	0.364	0.661	0.844	0.917
SimpleOcc [15]	Voxel	0.224	3.383	7.165	0.333	0.753	0.877	0.930
OccNeRF [62]	Voxel	0.202	2.883	6.697	0.319	0.768	0.882	0.931
SelfOcc [26]	Voxel	0.215	2.743	6.706	0.316	0.753	0.875	0.932
GaussianOcc [14]	Voxel	0.197	1.846	6.733	0.312	0.746	0.873	0.931
GaussianFlowOcc [7]	Gauss	0.278	2.522	5.232	0.389	0.677	0.826	0.898
MLGA	Quad	0.194	1.934	8.236	0.569	0.714	0.854	0.914
Gaussianisation	Quad	0.203	1.880	8.071	0.351	0.711	0.852	0.919
Voxel NeRF	Quad	0.208	2.023	8.383	0.387	0.683	0.822	0.894
SQOcc-R (Ours)	Quad	0.190	1.825	8.163	0.353	0.717	0.857	0.920

(b) Depth Estimation. Rep. denotes scene representation: Gauss - Gaussian; Quad - SuperQuadric.

For MLGA, Gaussianisation, and SuperQuadricOcc-Render, we used $4 \times$ A100 (40GB), and $4 \times$ H100 (80GB) for Voxel NeRF due to memory constraints.

For SQOcc-R, we use the implementation parameters stated in [subsection 4.2](#)

Quantitative evaluation

Semantic Occupancy. In [Table 3a](#), SuperQuadricOcc-Render achieves higher mIoU and significantly outperforms all other methods in RayIoU. MLGA attains worse results because the temporal flow module is disabled; enabling it leads to severely degraded performance. This can be attributed to the mismatch in decay between Gaussians (quadratic) and superquadrics (not necessarily quadratic), indicating that a Gaussian approximation is not appropriate for a render proxy.

On OpenOccv2, we improve upon Gaussianisation by 19.7% in RayIoU. During both training and inference, Gaussianisation requires less memory due to the efficiency of screen-space rasterisation. However, compared to Voxel NeRF, our method reduces memory usage by 92.9% during training and 74.7% during inference, owing to our spatial indexing strategy. Regarding rendering time, our method achieves performance comparable to Gaussianisation and reduces ren-

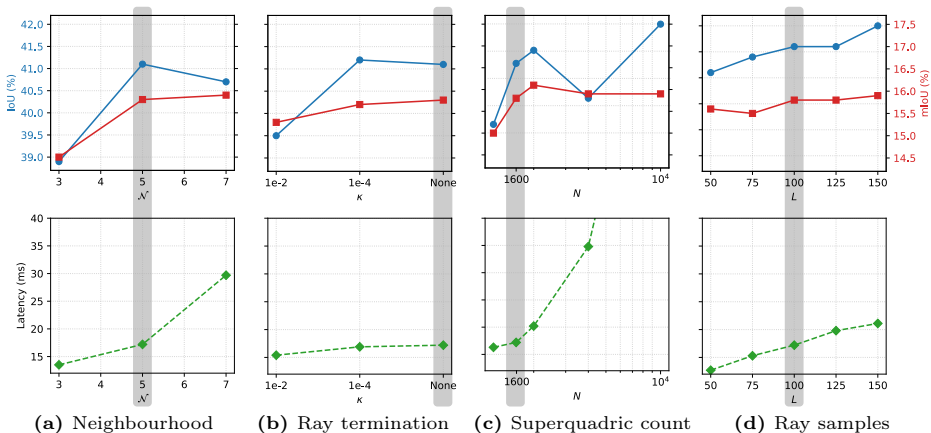


Fig. 3: Ablation studies on Occ3D-nuScenes [48] dataset. Metrics are IoU, mIoU and latency. From left to right, we study the neighbourhood size, the usage of ray termination, the number of superquadrics and the number of ray samples. The parameter highlighted in grey is the preferred value, corresponding to a compromise between prediction metrics and latency. The superquadric count is plotted with a x -log-scale.

der time by 83.2% compared to Voxel NeRF. MLGA lags behind SQOcc-R and Gaussianisation due to the large number of Gaussians (1M+) to render.

Depth Estimation. For superquadric-based depth estimation, in Table 3b (lower part), SQOcc-R outperforms the other approaches on all metrics except RMSE and RMSE log, where it performs on par with Gaussianisation. The overall improvements can be attributed to the direct rendering of superquadrics, which enables more accurate geometric reconstruction compared to the voxel-based proxy rendering employed by Gaussianisation and Voxel NeRF.

Additionally, we also report in the upper part of Table 3b, reference methods from the self-supervised literature for comparison, while not applicable to superquadric rendering. SQOcc-R achieves state-of-the-art performance on the Abs Rel and Sq Rel metrics among all methods, indicating improved geometric modelling of the scene. The comparatively higher RMSE suggests the presence of a limited number of larger depth deviations, potentially in distant regions, as restricting the depth perception range to 40m greatly reduces the RMSE from 8.163 to 4.444. Methods that incorporate photometric consistency losses alongside occupancy estimation [14, 15, 26, 62] tend to achieve stronger performance on threshold-based depth metrics; however, they severely underperform in occupancy estimation. Across the remaining metrics, our model remains competitive.

4.5 Ablation Studies

For the ablation study on SQOcc-R, we use the Occ3D-nuScenes [48] dataset. To reduce computational cost, we train on the first half of the dataset (300 scenes) and evaluate on the full validation set.

Neighbourhood Value \mathcal{N}_v : In Figure 3a, we ablate \mathcal{N}_v , which defines the cubic region around each superquadric within which ray samples are permitted to query it. Increasing \mathcal{N}_v improves performance, as each ray sample can consider a larger set of superquadrics, thereby enhancing rendering fidelity. However, we reach a saturation point at $\mathcal{N}_v = 7$. We therefore select $\mathcal{N}_v = 5$ to balance rendering fidelity, computational efficiency and rendering time.

Ray Termination κ : We ablate early ray termination in Figure 3b, which has been shown to accelerate rendering in prior work [36, 42]. Sampling along a ray stops once the accumulated transmittance T falls below a threshold κ . We observe that for $\kappa = 1e^{-2}$, performance degrades significantly, while for $\kappa = 1e^{-4}$ there is a small trade-off between performance metrics and latency. Thus, we choose not to apply early ray termination.

SuperQuadric Count N : In Figure 3c, we observe that at approximately 2,000 superquadrics, the model reaches a saturation point. Increasing N further provides minimal improvements in performance metrics while increasing render time. We find that render time increases linearly with increasing N count, and at $N = 10,000$ the latency reaches 91.6ms. Thus, we select 1,600 superquadrics to balance rendering cost and model inference speed.

Ray Sample Number L : Increasing the number of rays L improves performance metrics by enhancing rendering fidelity, seen in Figure 3d. Performance gains begin to saturate at approximately $L = 100$. While $L = 100$ yields the strongest overall results, using $L = 50$ remains competitive, with a 0.16 mIoU reduction and rendering time reduced by 26.2% compared to $L = 100$, making it a practical alternative depending on computational constraints.

4.6 Visualizations

Here, we present a visual analysis of semantic occupancy and depth estimation for GaussianFlowOcc [7] and four variants of SuperQuadricOcc.

In Figure 4, for semantic occupancy estimation, we examine that in the top scene, several models struggle to reconstruct a pole visible in the front camera image. SQOcc-R predicts a single, coherent pole structure, whereas GaussianFlowOcc and Gaussianisation under-predict the object, and MLGA and Voxel NeRF over-predict it. This observation reflects the challenges self-supervised models face when reconstructing small objects under occlusion. For the bottom scene, SQOcc-R correctly reconstructs the full car and surrounding vehicles, with GaussianFlowOcc notably struggling in this area.

For depth estimation in Figure 5, we consider a pole in the front left camera view. SQOcc-R produces a clearer and more complete reconstruction, while other methods capture the base of the pole but struggle to reconstruct its thinner upper structure. The single pedestrian in the back-left image is most clearly

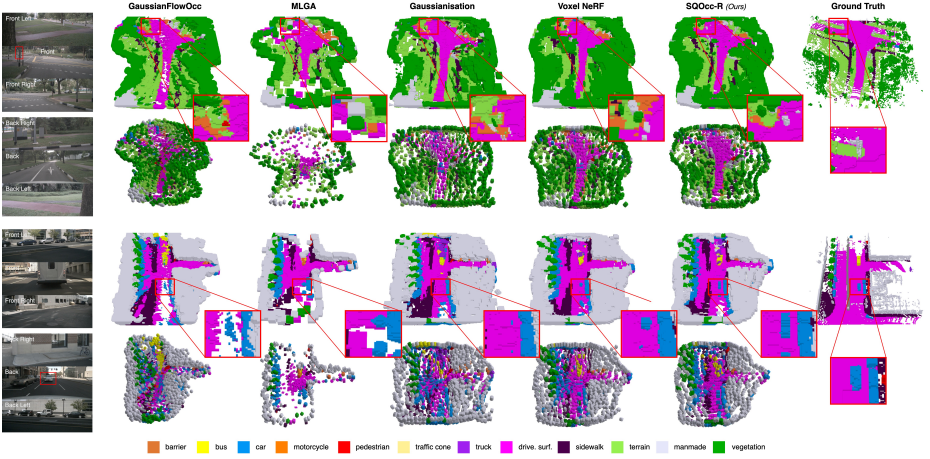


Fig. 4: Semantic Occupancy visual analysis. Best viewed zoomed in.

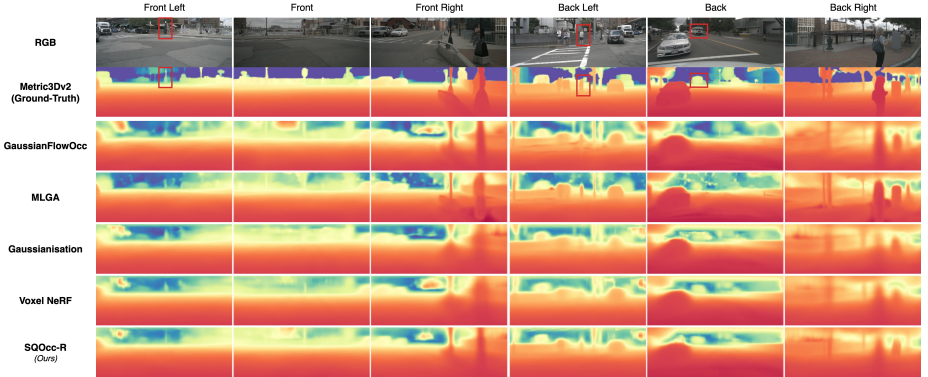


Fig. 5: Depth Estimation visual analysis. Best viewed zoomed in.

captured by GaussianFlowOcc, MLGA, and SQOcc-R, all of which render the scene directly, unlike methods that regress to voxel space. The bus in the back camera view is more clearly defined by SQOcc-R and Voxel NeRF. These results highlight the effectiveness of our direct rendering strategy in SQOcc-R.

5 Conclusion

In this paper, we present a real-time self-supervised occupancy model, SuperQuadricOcc, which uses superquadrics for scene representation to achieve state-of-the-art performance on the Occ3D-nuScenes dataset. To address the rendering challenge, we introduce a CUDA-accelerated superquadric renderer, SuperQuadricOcc-Render, that enables real-time rendering of thousands of superquadric primitives. Its spatial indexing strategy allows efficient querying of relevant superquadrics for each ray sample within the volume rendering framework, reduc-

ing rendering time while preserving fidelity, a limitation observed in alternative rendering approaches. Compared to other rendering methods, SuperQuadricOcc-Render consistently demonstrates superior results, achieving rendering speeds comparable to Gaussian-based methods. Overall, our results demonstrate the effectiveness of superquadric scene representations. They further show that efficient superquadric rendering is practical and can approach the performance of Gaussian rasterisation, encouraging further research into superquadric-based scene representations.

Acknowledgement

This publication has emanated from research conducted with the financial support of Taighde Éireann – Research Ireland under Grant number 18/CRT/6049. For the purpose of Open Access, the author has applied a CC BY public copyright licence to any Author Accepted Manuscript version arising from this submission.

References

1. Alaniz, S., Mancini, M., Akata, Z.: Iterative superquadric recomposition of 3d objects from multiple views. In: ICCV (2023) 3
2. Azinovič, D., Martin-Brualla, R., Goldman, D.B., Nießner, M., Thies, J.: Neural rgb-d surface reconstruction. In: CVPR (2022) 3
3. Barr, A.H.: Superquadrics and angle-preserving transformations. IEEE Computer graphics and Applications (1981) 4
4. Barsellotti, L., Bianchi, L., Messina, N., Carrara, F., Cornia, M., Baraldi, L., Falchi, F., Cucchiara, R.: Talking to dino: Bridging self-supervised vision backbones with language for open-vocabulary segmentation. In: ICCV (2025) 3
5. Batlle, V.M., Montiel, J.M., Fua, P., Tardós, J.D.: Lightneus: Neural surface reconstruction in endoscopy using illumination decline. In: MICCAI (2023) 3
6. Behley, J., Garbade, M., Milioto, A., Quenzel, J., Behnke, S., Stachniss, C., Gall, J.: Semantickitti: A dataset for semantic scene understanding of lidar sequences. In: ICCV (2019) 3
7. Boeder, S., Gigengack, F., Risse, B.: Gaussianflowocc: Sparse and weakly supervised occupancy estimation using gaussian splatting and temporal flow. In: ICCV (2025) 2, 3, 4, 7, 8, 9, 10, 11, 13, 21, 24, 28
8. Caesar, H., Bankiti, V., Lang, A.H., Vora, S., Liong, V.E., Xu, Q., Krishnan, A., Pan, Y., Baldan, G., Beijbom, O.: nuscenes: A multimodal dataset for autonomous driving. In: CVPR (2020) 3, 8, 10, 22
9. Chambon, L., Zablocki, E., Bouch, A., Chen, M., Cord, M.: Gaussrender: Learning 3d occupancy with gaussian rendering. In: ICCV (2025) 10
10. Chen, G., Wang, W.: A survey on 3d gaussian splatting. arXiv preprint arXiv:2401.03890 (2025) 3
11. Chen, Z., Yang, L., Lai, J.H., Xie, X.: Cunerf: Cube-based neural radiance field for zero-shot medical image arbitrary-scale super resolution. In: ICCV (2023) 3
12. Deng, J., Dong, W., Socher, R., Li, L.J., Li, K., Fei-Fei, L.: Imagenet: A large-scale hierarchical image database. In: CVPR (2009) 8

13. Deng, T., Chen, Y., Zhang, L., Yang, J., Yuan, S., Liu, J., Wang, D., Wang, H., Chen, W.: Compact 3d gaussian splatting for dense visual slam. arXiv preprint arXiv:2403.11247 (2024) [3](#)
14. Gan, W., Liu, F., Xu, H., Mo, N., Yokoya, N.: Gaussianocc: Fully self-supervised and efficient 3d occupancy estimation with gaussian splatting. In: ICCV (2025) [3](#), [8](#), [9](#), [10](#), [11](#), [12](#), [24](#)
15. Gan, W., Mo, N., Xu, H., Yokoya, N.: A simple attempt for 3d occupancy estimation in autonomous driving. CoRR (2023) [11](#), [12](#)
16. Gao, K., Gao, Y., He, H., Lu, D., Xu, L., Li, J.: Nerf: Neural radiance field in 3d vision, a comprehensive review. arXiv preprint arXiv:2210.00379 (2022) [3](#)
17. Gao, Z., Yi, R., Huang, Y., Chen, W., Zhu, C., Xu, K.: Self-supervised Learning of Hybrid Part-aware 3D Representations of 2D Gaussians and Superquadrics. In: ICCV (2025) [3](#), [10](#), [20](#)
18. Guédon, A., Lepetit, V.: Sugar: Surface-aligned gaussian splatting for efficient 3d mesh reconstruction and high-quality mesh rendering. In: CVPR (2024) [3](#), [20](#)
19. Hayes, S., Sistu, G., Eising, C.: EasyOcc: 3D Pseudo-Label Supervision for Fully Self-Supervised Semantic Occupancy Prediction Models. arXiv preprint arXiv:2509.26087 (2025) [9](#), [19](#)
20. He, K., Zhang, X., Ren, S., Sun, J.: Deep residual learning for image recognition. In: CVPR (2016) [8](#)
21. Hong, S., He, J., Zheng, X., Zheng, C.: Liv-gaussmap: Lidar-inertial-visual fusion for real-time 3d radiance field map rendering. In: RA-L (2024) [3](#)
22. Hou, J., Li, X., Guan, W., Zhang, G., Feng, D., Du, Y., Xue, X., Pu, J.: Fastocc: Accelerating 3d occupancy prediction by fusing the 2d bird’s-eye view and perspective view. In: ICRA (2024) [3](#)
23. Hu, L., Zhang, H., Zhang, Y., Zhou, B., Liu, B., Zhang, S., Nie, L.: Gaussianavatar: Towards realistic human avatar modeling from a single video via animatable 3d gaussians. In: CVPR (2024) [3](#)
24. Hu, M., Yin, W., Zhang, C., Cai, Z., Long, X., Chen, H., Wang, K., Yu, G., Shen, C., Shen, S.: Metric3d v2: A versatile monocular geometric foundation model for zero-shot metric depth and surface normal estimation. PAMI (2024) [3](#), [8](#), [20](#), [21](#)
25. Huang, Y., Thammatadatrakoon, A., Zheng, W., Zhang, Y., Du, D., Lu, J.: Gaussianformer-2: Probabilistic gaussian superposition for efficient 3d occupancy prediction. In: CVPR (2025) [3](#)
26. Huang, Y., Zheng, W., Zhang, B., Zhou, J., Lu, J.: Selfocc: Self-supervised vision-based 3d occupancy prediction. In: CVPR (2024) [3](#), [9](#), [11](#), [12](#)
27. Huang, Y., Zheng, W., Zhang, Y., Zhou, J., Lu, J.: Tri-perspective view for vision-based 3d semantic occupancy prediction. In: CVPR (2023) [3](#)
28. Huang, Y., Zheng, W., Zhang, Y., Zhou, J., Lu, J.: Gaussianformer: Scene as gaussians for vision-based 3d semantic occupancy prediction. In: ECCV (2024) [1](#), [3](#)
29. Jiang, H., Liu, L., Cheng, T., Wang, X., Lin, T., Su, Z., Liu, W., Wang, X.: Gausstr: Foundation model-aligned gaussian transformer for self-supervised 3d spatial understanding. In: CVPR (2025) [2](#), [3](#), [9](#), [24](#)
30. Jiang, S., Zhao, Q., Rahmani, H., Soh, D.W., Liu, J., Zhao, N.: Gaussianblock: Building part-aware compositional and editable 3d scene by primitives and gaussians. arXiv preprint arXiv:2410.01535 (2024) [3](#), [10](#), [20](#)
31. Jiang, Y., Shen, Z., Wang, P., Su, Z., Hong, Y., Zhang, Y., Yu, J., Xu, L.: Hifi4g: High-fidelity human performance rendering via compact gaussian splatting. In: CVPR (2024) [3](#)

32. Kerbl, B., Kopanas, G., Leimkühler, T., Drettakis, G.: 3D Gaussian splatting for real-time radiance field rendering. In: *ACM Trans. Graph.* (2023) 2, 3
33. Lee, J., Lee, Y., Kim, J., Kosiorek, A., Choi, S., Teh, Y.W.: Set transformer: A framework for attention-based permutation-invariant neural networks. In: *ICML* (2019) 4
34. Lee, S., Kang, W., Bertogna, M., Chwa, H.S., Lee, J.: Timing guarantees for inference of ai models in embedded systems. *Real-Time Systems* (2025) 29
35. Li, H., Gu, X., Yuan, W., Yang, L., Dong, Z., Tan, P.: Dense rgb slam with neural implicit maps. *arXiv preprint arXiv:2301.08930* (2023) 3
36. Li, R., Tancik, M., Kanazawa, A.: Nerfacc: A general nerf acceleration toolbox. *arXiv preprint arXiv:2210.04847* (2022) 13
37. Li, Z., Yu, Z., Austin, D., Fang, M., Lan, S., Kautz, J., Alvarez, J.M.: Fb-occ: 3d occupancy prediction based on forward-backward view transformation. *arXiv preprint arXiv:2307.01492* (2023) 3
38. Liao, Z., Wei, P., Chen, S., Wang, H., Ren, Z.: Stcocc: Sparse spatial-temporal cascade renovation for 3d occupancy and scene flow prediction. In: *CVPR* (2025) 3
39. Liso, L., Sandström, E., Yugay, V., Van Gool, L., Oswald, M.R.: Loopy-slam: Dense neural slam with loop closures. In: *CVPR* (2024) 3
40. Liu, Y., Li, C., Yang, C., Yuan, Y.: Endogaussian: Real-time gaussian splatting for dynamic endoscopic scene reconstruction. *arXiv preprint arXiv:2401.12561* (2024) 3
41. Ma, Q., Tan, X., Qu, Y., Ma, L., Zhang, Z., Xie, Y.: Cotr: Compact occupancy transformer for vision-based 3d occupancy prediction. In: *CVPR* (2024) 3
42. Müller, T., Evans, A., Schied, C., Keller, A.: Instant neural graphics primitives with a multiresolution hash encoding. *ACM TOG* (2022) 13
43. Oechsle, M., Peng, S., Geiger, A.: Unisurf: Unifying neural implicit surfaces and radiance fields for multi-view reconstruction. In: *ICCV* (2021) 3
44. Radford, A., Kim, J.W., Hallacy, C., Ramesh, A., Goh, G., Agarwal, S., Sastry, G., Askell, A., Mishkin, P., Clark, J., et al.: Learning transferable visual models from natural language supervision. In: *ICML* (2021) 3
45. Ren, T., Liu, S., Zeng, A., Lin, J., Li, K., Cao, H., Chen, J., Huang, X., Chen, Y., Yan, F., et al.: Grounded sam: Assembling open-world models for diverse visual tasks. *arXiv preprint arXiv:2401.14159* (2024) 3, 8, 20, 21
46. Rosinol, A., Leonard, J.J., Carlone, L.: Nerf-slam: Real-time dense monocular slam with neural radiance fields. In: *IROS* (2023) 3
47. Tang, P., Wang, Z., Wang, G., Zheng, J., Ren, X., Feng, B., Ma, C.: Sparseocc: Rethinking sparse latent representation for vision-based semantic occupancy prediction. In: *CVPR* (2024) 23
48. Tian, X., Jiang, T., Yun, L., Mao, Y., Yang, H., Wang, Y., Wang, Y., Zhao, H.: Occ3d: A large-scale 3d occupancy prediction benchmark for autonomous driving. *NeurIPS* (2023) 2, 3, 8, 9, 11, 12, 22, 24, 25, 26, 27, 29, 30, 34
49. Tong, W., Sima, C., Wang, T., Chen, L., Wu, S., Deng, H., Gu, Y., Lu, L., Luo, P., Lin, D., et al.: Scene as occupancy. In: *ICCV* (2023) 3, 8, 9, 11, 22, 29, 30
50. Waczyńska, J., Borycki, P., Tadeja, S., Tabor, J., Spurek, P.: Games: Mesh-based adapting and modification of gaussian splatting. *arXiv preprint arXiv:2402.01459* (2024) 3, 20
51. Wang, J., Liu, Z., Meng, Q., Yan, L., Wang, K., Yang, J., Liu, W., Hou, Q., Cheng, M.M.: Opus: occupancy prediction using a sparse set. *NeurIPS* (2024) 3

52. Wang, K., Yang, C., Wang, Y., Li, S., Wang, Y., Dou, Q., Yang, X., Shen, W.: Endogslam: Real-time dense reconstruction and tracking in endoscopic surgeries using gaussian splatting. In: MICCAI (2024) [3](#)
53. Wang, L., Kim, S.W., Yang, J., Yu, C., Ivanovic, B., Waslander, S., Wang, Y., Fidler, S., Pavone, M., Karkus, P.: Distillnerf: Perceiving 3d scenes from single-glance images by distilling neural fields and foundation model features. NeurIPS (2024) [9](#)
54. Wang, P., Liu, L., Liu, Y., Theobalt, C., Komura, T., Wang, W.: Neus: Learning neural implicit surfaces by volume rendering for multi-view reconstruction. arXiv preprint arXiv:2106.10689 (2021) [3](#)
55. Wang, X., Zhu, Z., Xu, W., Zhang, Y., Wei, Y., Chi, X., Ye, Y., Du, D., Lu, J., Wang, X.: Openoccupancy: A large scale benchmark for surrounding semantic occupancy perception. In: ICCV (2023) [3](#), [22](#)
56. Wang, Y., Long, Y., Fan, S.H., Dou, Q.: Neural rendering for stereo 3d reconstruction of deformable tissues in robotic surgery. In: MICCAI (2022) [3](#)
57. Wei, Y., Zhao, L., Zheng, W., Zhu, Z., Rao, Y., Huang, G., Lu, J., Zhou, J.: Surrounddepth: Entangling surrounding views for self-supervised multi-camera depth estimation. In: CoRL (2023) [11](#)
58. Wei, Y., Zhao, L., Zheng, W., Zhu, Z., Zhou, J., Lu, J.: Surroundocc: Multi-camera 3d occupancy prediction for autonomous driving. In: ICCV (2023) [3](#), [22](#)
59. Xiao, W., Chierchia, R., Cruz, R.S., Li, X., Ahmedt-Aristizabal, D., Salvado, O., Fookes, C., Lebrat, L.: Neural radiance fields for the real world: A survey. arXiv preprint arXiv:2501.13104 (2025) [3](#)
60. Ye, V., Li, R., Kerr, J., Turkulainen, M., Yi, B., Pan, Z., Seiskari, O., Ye, J., Hu, J., Tancik, M., et al.: gsplat: An open-source library for Gaussian splatting. Journal of Machine Learning Research (2025) [29](#)
61. Yu, Z., Liu, Q., Wang, W., Zhang, L., Zhao, X.: Superocc: Toward cohesive temporal modeling for superquadric-based occupancy prediction. arXiv preprint arXiv:2601.15644 (2026) [1](#), [3](#)
62. Zhang, C., Yan, J., Wei, Y., Li, J., Liu, L., Tang, Y., Duan, Y., Lu, J.: Occnerf: Self-supervised multi-camera occupancy prediction with neural radiance fields. CoRR (2023) [2](#), [3](#), [9](#), [10](#), [11](#), [12](#)
63. Zhang, F., Yang, H., Zhang, Z., Huang, Z., Luo, Y.: Tt-occ: Test-time compute for self-supervised occupancy via spatio-temporal gaussian splatting. arXiv preprint arXiv:2503.08485 (2025) [3](#), [8](#), [9](#), [24](#)
64. Zhang, H., Li, F., Zou, X., Liu, S., Li, C., Yang, J., Zhang, L.: A simple framework for open-vocabulary segmentation and detection. In: ICCV (2023) [3](#)
65. Zhao, L., Wei, S., Hays, J., Gan, L.: GaussianFormer3D: Multi-Modal Gaussian-based Semantic Occupancy Prediction with 3D Deformable Attention. arXiv preprint arXiv:2505.10685 (2025) [3](#)
66. Zuo, S., Zheng, W., Han, X., Yang, L., Pan, Y., Lu, J.: Quadricformer: Scene as superquadrics for 3d semantic occupancy prediction. arXiv preprint arXiv:2506.10977 (2025) [1](#), [3](#), [4](#), [24](#)
67. Zuo, S., Zheng, W., Huang, Y., Zhou, J., Lu, J.: Pointocc: Cylindrical tri-perspective view for point-based 3d semantic occupancy prediction. arXiv preprint arXiv:2308.16896 (2023) [3](#)
68. Zuo, S., Zheng, W., Huang, Y., Zhou, J., Lu, J.: Gaussianworld: Gaussian world model for streaming 3d occupancy prediction. In: CVPR (2025) [3](#)

SuperQuadricOcc: Real-Time Self-Supervised Semantic Occupancy Estimation with Superquadric Volume Rendering

Supplementary Material

Overview

We divide the supplementary material into three sections:

1. **Supplementary Information:** In [section A](#), we provide additional details that assist the reader in understanding concepts not included in the main paper, such as the formulation of evaluation metrics.
2. **Supplementary Ablations:** In [section B](#), we present additional ablation studies that offer further insight into the rendering methods used in SuperQuadricOcc, specifically SuperQuadricOcc-Render.
3. **Supplementary Visualisations:** In [section C](#), we include additional visualisations of SuperQuadricOcc.

A Supplementary Information

In this section, we provide additional information that could not be included in the main paper due to length constraints, including a discussion on the limitations and future work.

A.1 Limitations and Future Work

In this section, we discuss the limitations and future directions of our proposed model, SuperQuadricOcc (SQOcc), as well as those of the rendering methods, with particular focus on SuperQuadricOcc-Render (SQOcc-R).

In SQOcc, the use of superquadrics improves performance metrics while reducing inference time. However, incorporating 3D pseudo-labels alongside our rendering pipeline could further enforce spatial consistency [19]. Additional work on constraining certain class types to specific epsilon ϵ and scale s ranges may help the model develop a more structured representation, which could further reduce the number of primitives required.

In SQOcc-R, we observe that the backward pass is a major bottleneck during training, as shown in [Table 11](#), due to the large number of atomic additions. Further optimisation could significantly reduce training time. Within the spatial indexing strategy, incorporating the superquadric occupancy probability into the indexing process may reduce inference time by avoiding queries to superquadrics with low opacity or rapidly decaying influence. However, this may introduce

challenges, as it could result in a dynamic number of superquadrics per voxel, disrupting the batching mechanism that currently enables efficient computation.

Future work on a native superquadric rasteriser would allow direct screen-space rendering, enabling faster and more accurate rendering. This would remove the need for a Gaussian or voxel rendering proxy and may lead to improved performance compared with SQOcc-R.

A.2 Problem Statement

The task of semantic occupancy estimation aims to predict the semantic class $\mathcal{C} = \{c_0, c_1, \dots, c_n\}$ for each voxel in a discretised 3D space using a model M . For the nuScenes dataset, the model may utilise surround-view camera images, LiDAR, radar, or a combination of these modalities. Let the input data over a temporal horizon $T = \{t - n, \dots, t\}$ be denoted as $D_n = \{D_{t-n}, \dots, D_t\}$. The model processes this sequence as $M(D_n)$ to produce a scene representation. The form of the output depends on the chosen representation and stage of operation, and may consist of voxel grids, Gaussian primitives, or superquadrics.

In our self-supervised approach, SQOcc outputs a set of refined superquadric primitives \mathcal{S} . During training, \mathcal{S} is rendered, and losses are computed against 2D pseudo-labels generated by VFMs [24, 45]. During inference, the superquadrics are voxelised, and evaluation metrics are computed against dense ground-truth voxel grids.

A.3 Multi-Layer Gaussian Approximation

The design of the Multi-Layer Gaussian Approximation (MLGA) is discussed in the main paper in Section 4.4. Here, we provide additional detail on its implementation.

As described in the main paper, the goal of MLGA is to approximate the superquadric occupancy probability function $p_o(\mathbf{x}, S)$ for an arbitrary superquadric S using a set of Gaussians. We first reduce S to its canonical form $S = (\mathbf{s}, \varepsilon_1, \varepsilon_2)$, and later apply translation and rotation to place it in world space. Our implementation follows PartGS [17] and GaussianBlock [30], which builds upon SuGaR [18], and GaMeS [50], methods that place Gaussians on mesh surfaces.

We begin by augmenting the scale parameters of S with n positive scalars $P = \{p_1, p_2, \dots, p_n\} \subset \mathbb{R}^+$ to define a scaled family of superquadrics: $S_P = \{(p\mathbf{s}, \varepsilon_1, \varepsilon_2) \mid p \in P\}$. This produces a layered superquadric structure analogous to level sets.

Following PartGS [17], for $S_p \in S_P$, we construct a superquadric mesh by first generating an icosphere. Let (x, y, z) denote the vertices of the icosphere. For each vertex, we compute the spherical parameters $\eta = \arcsin(y)$ and $\omega = \text{atan2}(x, z)$. The vertex is then mapped onto the superquadric surface using signed powers of trigonometric functions controlled by ε_1 and ε_2 :

$$\mathbf{v} = [s_1 \cos^{\varepsilon_1}(\eta) \cos^{\varepsilon_2}(\omega), s_2 \sin^{\varepsilon_1}(\eta), s_3 \cos^{\varepsilon_1}(\eta) \sin^{\varepsilon_2}(\omega)]. \quad (9)$$

For each face V with vertices $v_1, v_2, v_3 \in \mathbb{R}^3$, instantiate a Gaussian G with mean \mathbf{m}_G as the centroid of the face. The Gaussian rotation R_G is defined by constructing orthonormal vectors $r_1, r_2, r_3 \in \mathbb{R}^3$ to form the rotation matrix $R_G = [r_1, r_2, r_3]$.

The vector r_1 is aligned with the normal vector of V , while r_2 is defined as the vector from the centroid of the triangle to the first vertex v_1 . The third vector r_3 is obtained by orthonormalising the vector from the centroid to the second vertex with respect to r_1 and r_2 :

$$r_2 = \frac{v_1 - m}{\|v_1 - m\|}, \quad r_3 = \frac{\text{ort}(v_2 - m; r_1, r_2)}{\|\text{ort}(v_2 - m; r_1, r_2)\|}, \quad (10)$$

where ort denotes orthonormalisation using the Gram–Schmidt process. For the Gaussian scale S_G , we assign $s_x = \|m - v_1\|$ and $s_y = \langle v_2, r_3 \rangle$, allowing the Gaussians to adequately cover the vertex face.

We build upon previous works, extending this approximation to 3D space by introducing a z scale s_z . For a Gaussian G_p with centre \mathbf{x}_p sampled on superquadric S_p , we define a corresponding Gaussian \mathbf{x}_{p+1} on S_{p+1} at the same angular coordinates (η, ω) and assign s_z as half the euclidean distance:

$$s_z = \frac{1}{2} \|\mathbf{x}_{p+1}(\eta, \omega) - \mathbf{x}_p(\eta, \omega)\|. \quad (11)$$

This assignment enables the Gaussians to model the space between scaled superquadrics, producing a more uniform density. The final Gaussian scale S_G is then defined as:

$$S_G = \text{diag}(s_x, s_y, s_z), \quad (12)$$

Previous works assign the Gaussian opacity directly from the parent superquadric. In our case, since Gaussians are used to model occupancy probability, we instead define:

$$\sigma = \sigma_{S_p} \cdot e^{f(\mathbf{m})}. \quad (13)$$

This scaling aligns the Gaussian occupancy with that of the superquadric, ensuring that the occupancy evaluated at the Gaussian centre matches the corresponding value in the superquadric distribution.

Finally, all Gaussians are transformed into the world coordinate system using rotation and translation defined by the parent superquadric mean \mathbf{m} and quaternion \mathbf{r} .

A.4 Loss Formulation

For fair comparison, we adopt the full loss formulation of GaussianFlowOcc [7]. Supervision uses 2D pseudo-labels from VFMs: Grounded-SAM [45] for semantics (S) and Metric3Dv2 [24] for depth (D). During training, the chosen render method provides rendered semantics (\hat{S}) and depth (\hat{D}). The semantic loss \mathcal{L}_{sem} is cross-entropy with $\lambda_s = 2$, and the depth loss $\mathcal{L}_{\text{depth}}$ is MSE with $\lambda_d = 0.05$. The full loss formulation is provided in Equation (14). Training is performed using Adam with a learning rate of 10^{-4} .

$$\mathcal{L} = \lambda_s \mathcal{L}_{\text{sem}}(\hat{S}, S) + \lambda_d \mathcal{L}_{\text{depth}}(\hat{D}, D) \quad (14)$$

A.5 Datasets

nuScenes [8]: The nuScenes dataset contains 1000 scenes of urban driving collected in Boston and Singapore. The ego-vehicle is equipped with six surround-view cameras, one 32 laser LiDAR sensor, and five radar sensors. The dataset is split into 700 scenes for training, 150 for validation, and 150 unannotated scenes for testing. Each scene contains approximately 40 key frames, representing around 20 seconds of driving. For each annotated key frame, ground-truth 3D bounding boxes and BEV labels are provided to support training and validation.

For nuScenes-lidarseg, each LiDAR point cloud is manually annotated with a semantic class. This, alongside the previously mentioned ground-truth labels enable the construction of dense 3D occupancy datasets.

Occ3D [48]: The Occ3D dataset follows the design of earlier occupancy datasets [55, 58], using multi-frame aggregation to densify the point cloud for each sample. Additional refinements, including occlusion reasoning and image guidance, are applied to generate higher-quality ground-truth labels. The dataset contains 600 scenes for training and 150 for validation. The evaluation space spans $[-40\text{m}, 40\text{m}]$ along the X and Y axes and $[-1\text{m}, 5.4\text{m}]$ along the Z axis, with a voxel resolution of 0.4m^3 , defined in the ego-vehicle coordinate frame.

Occ3D is the most widely used dataset for evaluating self-supervised models, largely due to the inclusion of a camera mask that restricts the evaluation space to regions visible in the camera views. However, the RayIoU metric also enables similar evaluation on other datasets.

OpenOccv2 [49]: This dataset provides occupancy labels in a similar manner to Occ3D, using multi-frame LiDAR aggregation, with an equivalent evaluation space and number of scenes. It provides denser occupancy labels with reduced noise due to dedicated noise removal, which more effectively penalises models that overpredict. This dataset does not include a camera mask, and therefore, we do not report IoU or mIoU; instead, we report RayIoU.

A.6 Evaluation Metrics

For semantic occupancy evaluation, we use three standard metrics: IoU, mIoU, and RayIoU. For depth evaluation, we use Abs Rel, Sq Rel, RMSE, RMSE log, and threshold accuracy metrics (δ).

Intersection over Union (IoU): For IoU, we first convert the semantic voxel grid into a binary grid by assigning the *free* class to 0 and all other classes to 1. The IoU formula is given as follows:

$$\text{IoU} = \frac{TP}{TP + FP + FN} \quad (15)$$

where TP , FP , and FN denote true positives, false positives, and false negatives, respectively. IoU measures the model’s ability to estimate occupancy and is traditionally less preferred since it does not penalise semantic misclassifications, which are important in automotive perception.

Mean Intersection over Union (mIoU): This metric is more commonly used as it properly penalises misclassifications, providing a better measure of the model’s ability to estimate both occupancy and semantic class. The formulation is given as follows:

$$\text{mIoU} = \frac{1}{C} \sum_{c=1}^C \frac{TP_c}{TP_c + FP_c + FN_c} \quad (16)$$

where C denotes the total number of semantic classes. The empty class $c = 0$ is excluded from the calculation.

RayIoU: First introduced in SparseOcc [47], this metric addresses issues such as over-penalisation and over-prediction that can artificially inflate mIoU scores while not accurately reflecting overall scene completion. RayIoU operates by projecting rays from the LiDAR viewpoint into the ground-truth voxel grid and traversing them until a voxel is intersected. The same ray is then projected into the predicted voxel grid. A true positive is assigned if the semantic class matches and the L1 distance between the ground-truth ray and predicted ray is within a defined threshold. The formulation is similar to that of mIoU:

$$\text{RayIoU} = \frac{1}{C} \sum_{c=1}^C \frac{TP_c}{TP_c + FP_c + FN_c} \quad (17)$$

Depth Metrics: We use the depth metrics adopted in previous works to evaluate depth estimation accuracy:

1. **Abs Rel:** $\frac{1}{|T|} \sum_{d \in T} \frac{|d - d^*|}{d^*}$
2. **Sq Rel:** $\frac{1}{|T|} \sum_{d \in T} \frac{|d - d^*|^2}{d^{*2}}$
3. **RMSE:** $\sqrt{\frac{1}{|T|} \sum_{d \in T} |d - d^*|^2}$
4. **RMSE_{log}:** $\sqrt{\frac{1}{|T|} \sum_{d \in T} |\log d - \log d^*|^2}$
5. $\delta < t$: percentage of d such that $\max\left(\frac{d}{d^*}, \frac{d^*}{d}\right) < t$

where d denotes the ground-truth depth map, d^* denotes the predicted depth map, and T represents the total number of evaluated pixels.

Table 4: Gaussian/SuperQuadric primitive count comparison. * GaussianOcc uses Gaussians during training only, converting each voxel to a Gaussian. The remaining models are for training and inference.

Method	Representation	Primitives
TT-Occ [63]	Gaussian	2,968,647
GaussianOcc* [14]	Gaussian	640,000
GaussianFlowOcc [7]	Gaussian	10,000
GaussTR [29]	Gaussian	1,800
SQOcc (Ours)	SuperQuadric	1,600

A.7 Primitive Count

In Table 4, we compare the total primitive count across various models, highlighting the efficiency of SQOcc’s scene representation through the use of superquadrics.

Many Gaussian-based models employ large numbers of Gaussian primitives. For example, TT-Occ [63] uses a large primitive count due to its strategy of initialising Gaussians on a pixel basis. GaussTR uses fewer primitives; however, it relies heavily on large foundation models during inference, which significantly limits real-time deployment. In contrast, SQOcc requires relatively few superquadric primitives due to their expressive shape family, enabling compact scene modelling. Combined with our efficient rendering proxy used for supervision, this results in improved performance compared with previous methods.

A.8 Scale and Epsilon Constraints

We constrain the scale \mathbf{s} to the range $[0, 1]$, following previous works [7]. For the epsilon parameters ϵ , we restrict their range to $[0.1, 2.0]$, consistent with prior work [66].

B Supplementary Ablations

In this section, we present additional ablation results for SuperQuadricOcc, focusing on the rendering pipelines used for supervision.

B.1 Rendering Ablation Studies

We evaluate our ablations on the Occ3D-nuScenes [48] dataset. To reduce computational cost, we train Gaussianisation, Voxel NeRF, and SQOcc-R on the first half of the dataset (300 scenes) and evaluate them on the full validation set. MLGA is trained on the full dataset, as it trains significantly faster without the temporal module.

Table 5: Multi-Layer Gaussian Approximation (MLGA) ablation studies on Occ3D-nuScenes [48] dataset. The parameter highlighted in grey is the preferred value, corresponding to a compromise between prediction metrics and latency. Lat. denotes latency, the average time to render each sample of the entire validation set, measured in milliseconds. The best-performer is highlighted in **bold**.

(a) Icosphere Faces					(b) Gaussian z-scale s_z				(c) Scale Gaussian Opacity			
Level	Faces	IoU	mIoU	Lat.	s_z	IoU	mIoU	Lat.	Scale Opacity	IoU	mIoU	Lat.
0	20	32.24	12.66	35.98	0.01	33.16	12.60	43.87	✓	33.67	12.69	44.04
1	80	33.67	12.69	44.04	0.1	29.74	11.32	44.27	✗	22.70	8.23	40.58
2	320	33.26	12.29	73.00	Half-Euclidean	33.67	12.69	44.04				
3	1280	OOM	OOM	OOM								

(d) SuperQuadric Count				(e) Scale Values						
N	IoU	mIoU	Lat.	Scale Values				IoU	mIoU	Lat.
1200	32.05	12.44	35.30	[0.5, 0.6, 0.75, 0.9, 1.05, 1.2, 1.6, 2.0, 2.5]				33.67	12.69	44.04
1600	33.67	12.69	44.04	[0.1, 0.22, 0.40, 0.58, 0.76, 0.94, 1.42, 1.90, 2.5]				32.88	12.37	40.10
2000	33.99	12.70	44.73	[0.5, 0.65, 0.88, 1.1, 1.33, 1.55, 2.15, 2.75, 3.5]				32.53	12.19	49.40
5000	27.77	6.95	60.45	[0.5, 0.7, 0.9, 1.1, 1.3, 1.5, 1.7, 1.9, 2.1, 2.3, 2.5]				33.78	12.50	51.44
10000	27.85	4.59	121.41							

Multi-Layer Gaussian Approximation (MLGA): Here, we investigate several components of the MLGA superquadric approximation proposed in the main paper.

Icosphere Faces: Table 5a examines the number of faces per scaled superquadric in the superquadric-to-Gaussian module. Results show that using 80 faces per scaled superquadric provides the best balance, offering sufficient surface coverage without the computational overhead observed with 320 faces. Using 20 faces may also be considered effective, as it results in only a 0.03 decrease in mIoU while reducing latency. Notably, configurations with 1280 faces result in an out-of-memory error.

Gaussian z-scale s_z : Table 5b evaluates the formulation of the Gaussian z-scale s_z . Assigning the z-scale as half the Euclidean distance to corresponding Gaussians produces higher performance than using a constant scale. Similar to the opacity scaling ablation, this results in a more accurate density distribution within the superquadric, improving supervision quality. Latency remains approximately the same across all variants.

Scaling of Gaussian Opacity: Table 5c evaluates the inclusion of the superquadric scaling term, $e^{f(m)}$, in the Gaussian opacity formulation. Including this term improves performance by enabling Gaussians to better approximate the superquadric distribution, resulting in a more consistent supervision signal. Not using scale opacity reduces render time, likely due to fewer superquadrics appearing in the camera view as a result of less complete scene reconstruction, as indicated by the results.

Superquadric Count N : In Table 5d, at lower primitive counts (>2000), the MLGA strategy provides effective supervision. However, when the primitive

Table 6: Gaussianisation and Voxel NeRF ablation studies on Occ3D-nuScenes [48] dataset. The parameter highlighted in grey is the preferred value, corresponding to a compromise between prediction metrics and latency. Lat. denotes latency, the average time to render each sample of the entire validation set, measured in milliseconds. The best-performer is highlighted in **bold**.

(a) Gaussian scale s				(b) Voxel NeRF ray samples L			
s	IoU	mIoU	Latency (ms)	L	IoU	mIoU	Latency (ms)
0.15	43.14	16.04	13.78	50	33.01	12.10	86.52
0.20	42.20	16.04	15.29	75	33.27	12.21	113.31
0.28	40.47	15.46	15.58	100	32.31	11.67	133.90
0.40	36.60	14.34	15.49	125	33.56	11.87	145.32
				150	32.87	11.79	159.98

count exceeds 2000, performance degrades significantly, possibly due to confusion in the render proxy caused by excessive overlapping superquadrics and therefore Gaussians. We note this as a key limitation of this method. Choosing $N = 1600$ provides the best balance between model performance and render time.

Scale Values: Table 5e studies the effect of different scale values for the scaled family of superquadrics, S_K . We observe that configurations emphasising interior layers of the superquadric achieve better performance, as these regions exhibit higher density. For example, using a fixed scale difference of 0.2 leads to worse results due to insufficient emphasis on interior layers. In contrast, overemphasising either interior or exterior layers degrades performance, likely due to sparser sampling and a mismatch between Gaussian and superquadric density distributions.

Gaussianisation and Voxel NeRF Here, we investigate the optimal Gaussian scale s and the Voxel NeRF ray sample number L .

For the Gaussian scale ablation in Table 6a, we find that a constant scale of 0.15 across all three axes produces the best results for IoU, mIoU, and rendering latency. This scale is slightly below the voxel radius $0.20m$, allowing sufficient decay outside the voxel and resulting in a more accurate rendering compared with larger scale values.

For the ray sample number L , the model must be trained without temporal labels, as using $L > 75$ results in an out-of-memory error, highlighting a limitation of voxel-based volume rendering. We observe in Table 6b that $L = 75$ provides the best balance between model performance and rendering speed. Interestingly, for $L > 75$, performance decreases, which differs from the behaviour observed in SQOcc-R, where results examine diminishing returns. This may indicate instability during training with Voxel NeRF.

Table 7: SuperQuadricOcc-Render ablation studies on Occ3D-nuScenes [48]. The parameter highlighted in grey is the preferred value, corresponding to a compromise between prediction metrics and latency. Lat. denotes latency, the average time to render each sample of the entire validation set, measured in milliseconds. The best-performer is highlighted in **bold**.

N	IoU	mIoU	Lat.	κ	IoU	mIoU	Lat.	N	IoU	mIoU	Lat.	L	IoU	mIoU	Lat.
3	38.86	14.53	13.54	$1e^{-2}$	39.45	15.24	15.36	1,200	39.69	14.96	16.33	50	40.61	15.64	12.68
5	41.10	15.80	17.18	$1e^{-4}$	41.15	15.69	16.86	1,600	41.10	15.80	17.18	75	40.89	15.49	15.30
7	40.65	15.88	29.73	None	41.10	15.80	17.18	2,000	41.36	16.08	20.16	100	41.10	15.80	17.18
								4,000	40.24	15.92	34.84	125	41.14	15.83	19.77
								10,000	42.00	15.86	91.18	150	41.53	15.85	21.12

(a) Neighbourhood value N (b) Ray termination value κ (c) Superquadric total N (d) Ray samples L

SuperQuadricOcc-Render: In Table 7, we present the ablation results shown in Figure 3 of the main paper, now including numerical values for completeness. A discussion of these results is provided in the main paper.

B.2 Rendering Method Robustness

To evaluate the robustness of each rendering method, we ablate them under varying image and voxel resolutions, and additionally study Voxel-NeRF and SQOcc-R with different ray sample counts L .

Table 8: Render time for varying image and voxel grid resolutions: We take the best performing fully trained model from the main results section. Default image resolution is set to 256x704, default voxel resolution is set to 200x200x16. OOM denotes out of memory on a 40GB NVIDIA A100 GPU. Metrics are expressed in milliseconds.

Method	Image Resolution			Voxel Resolution		
	128x352	256x704	512x1408	200x200x16	300x300x24	400x400x32
MLGA	26.99	44.04	66.88	44.04	44.04	44.04
Gaussianisation	14.12	15.50	29.64	15.50	48.62	95.86
Voxel NeRF	56.41	102.44	OOM	102.44	137.23	164.47
SQOcc-R (Ours)	10.06	17.66	47.36	17.66	17.66	17.66

Image and Voxel Resolution: In Table 8, we observe that Voxel NeRF struggles with increasing image resolution, particularly at larger resolutions where it runs out of memory. Both Gaussianisation and SQOcc-R perform well under these conditions, with Gaussianisation achieving better results at larger image resolutions due to efficient screen-space rasterisation. However, our method shows lower rendering time at smaller resolutions. For increased voxel resolutions, both Gaussianisation and Voxel-NeRF struggle significantly, especially Gaussianisation, which requires one Gaussian per voxel, highlighting a limitation of the

approach. In contrast, SQOcc-R and MLGA maintain consistent rendering time regardless of voxel resolution, as they do not regress to voxel space.

Table 9: Memory and Latency comparison. We take the best performing fully trained model from the main results section and ablate the ray sample number L during inference render time. The best result in each column is highlighted in **bold**.

Metric	Method	Ray Samples L						
		50	75	100	125	150	175	200
Memory (GB)	Voxel NeRF	7.53	11.14	14.75	18.36	21.97	25.58	29.19
	SQOcc-R (Ours)	1.57	2.19	2.81	3.43	4.05	4.67	5.29
Latency (ms)	Voxel NeRF	88.044	102.44	126.09	141.03	153.23	167.74	178.38
	SQOcc-R (Ours)	13.33	15.22	17.20	20.22	22.28	24.45	25.95

Ray Sample Number L : In Table 9, we compare Voxel-NeRF and SQOcc-R across varying ray sample counts L in terms of memory usage and latency. SQOcc-R consistently maintains approximately an 84% reduction in latency and around an 80% reduction in memory across all tested values of L . Comparing the $400 \times 400 \times 32$ voxel resolution used by Gaussianisation with $L = 200$ in SQOcc-R provides a comparable scene resolution. In this case, SQOcc-R significantly outperforms in latency, reducing rendering time from 96ms to 26ms. This demonstrates that our method scales more effectively with increasing scene resolution.

B.3 Scalability of Methods

Here, we compare the methods when trained with 10,000 superquadric primitives. We observe that Gaussianisation outperforms our method, SQOcc-R, in terms of mIoU and render time. However, it performs worse in RayIoU compared to SQOcc-R on OpenOccv2, which was also observed in the main paper. This suggests limitations in overall scene completion for this method and indicates a saturation point in superquadric count, similar to the behaviour reported in GaussianFlowOcc [7] when the Gaussian count exceeds their saturation point of 10,000.

Voxel NeRF encounters an out-of-memory error (80GB+), due to the already high memory requirements of the method. With increased GPU memory, training may become feasible, as inference does not require the rendering method to be used. MLGA performance decreases significantly, indicating limitations with the render proxy under this configuration.

We note that comparisons with the fully trained 1,600 superquadric models are not strictly fair, as the models in this study are trained using only half of the dataset, following the ablation study setup.

Table 10: Training with 10,000 SuperQuadrics Voxel-NeRF contains no values as we are met with an out-of-memory error during training. Models are trained with half the training dataset, as done in the ablation studies. The best result overall is highlighted in **bold**.

Method	IoU	mIoU	RayIoU		Latency (ms)	Memory (GB)
			Occ3D [48]	OpenOccv2 [49]		
MLGA	27.85	4.59	2.85	3.45	121.41	4.42
Gaussianisation	43.44	17.45	14.51	15.41	65.30	3.72
Voxel NeRF	-	-	-	-	-	-
SQOcc-R (Ours)	42.00	15.86	14.46	15.98	91.18	3.43

B.4 Training Information

In Table 11, we examine the training time along with forward and backward pass times for all four render methods.

Table 11: Training information: Training time is measured while training on $4 \times$ H100 (80GB) for fairness and due to memory constraints issues with Voxel NeRF. All methods are trained with the temporal flow module enabled for equal comparison. Models are trained for 18 epochs. Forward and Backward denote the average time to process each sample during training.

Method	Parameters	Training Time	Forward (ms)	Backward (ms)
MLGA	35.7M	1d 21hr	0.221	0.148
Gaussianization	35.7M	1d 19hr	0.243	0.110
Voxel NeRF	35.7M	2d 4hr	0.587	0.865
SQOcc-R	35.7M	3d 5hr	0.238	1.828

We observe that Gaussian-based methods (MLGA, Gaussianisation) require the shortest training time due to the efficiency of Gaussian rasterisation and the implementation provided by the gsplat library [60]. Volume rendering-based methods (Voxel NeRF, SQOcc-R) require noticeably longer training times, particularly SQOcc-R. However, SQOcc-R achieves the second fastest forward pass among all approaches, while the backward pass is significantly slower, contributing to the longer training time. This is caused by the large number of atomic additions required to backpropagate gradients from ray samples to the superquadric parameters. We identify this as a current limitation of SQOcc-R, though it could be addressed through more efficient optimisation.

Despite this, SQOcc-R achieves higher performance metrics, which is particularly important for real-time systems, particularly automotive systems that require safety and reliability guarantees [34].

B.5 Training on the Same GPU Architecture

In Table 12, we train all models on the same GPU architecture for fairness: 4× 80GB NVIDIA H100 GPUs. As mentioned in the main paper, we trained only Voxel NeRF on the 80GB NVIDIA H100 GPUs due to memory constraints.

Table 12: Training on the same GPU Architecture We train the models again on 4 80GB NVIDIA H100. The best result overall is highlighted in **bold**.

Model	IoU	mIoU	RayIoU	
			Occ3D [48]	OpenOccv2 [49]
MLGA	34.48	12.72	11.82	13.48
Gaussianization	43.73	16.97	15.00	16.13
Voxel NeRF	42.94	17.10	16.56	17.72
SQOcc-R (Ours)	43.25	17.04	16.98	18.52

Here, we observe trends similar to those reported in the main paper. Gaussianisation, Voxel NeRF, and SQOcc-R show comparable performance across IoU and mIoU. For RayIoU, which is less sensitive to depth estimation errors and penalises over-prediction, SQOcc-R outperforms the other methods, consistent with the results in the main paper. This is particularly evident on OpenOccv2 [49], which provides denser occupancy labels compared to Occ3D [48].

B.6 Self-Supervised Pre-Training

To further evaluate the effectiveness of our SQOcc-R rendering module, we train SQOcc using ground-truth voxel labels without pre-training for 18 epochs, and then repeat the experiment using pre-trained weights obtained from SQOcc-R.

Table 13: Effect of pre-training a strongly-supervised model: We train SuperQuadricOcc with ground-truth labels, and compare it to a model pre-trained with self-supervision from SQOcc-R. The best result overall is highlighted in **bold**.

Supervision	Pretraining	IoU	mIoU	RayIoU	
				Occ3D [48]	OpenOccv2 [49]
Strong	None	55.25	24.37	15.57	17.65
Strong	SQOcc-R	57.65	29.16	20.76	23.35

We observe a noticeable improvement in model performance, particularly for RayIoU, where there is a 33.3% increase on the Occ3D dataset and a 32.3% increase on the OpenOccv2 dataset. This highlights the benefit of using pre-trained weights and suggests that self-supervised occupancy estimation can further support supervised occupancy estimation.

B.7 SuperQuadric Decay for Neighbourhood Values \mathcal{N}

In Table 14, we examine the value of the superquadric occupancy distribution, $p_o(\mathbf{x}, S)$, for all predicted superquadrics in the validation set for SuperQuadricOcc trained with SQOcc-R. We compute the average value across all superquadrics for three points corresponding to the maximum distances within the cubic neighbourhood: the maximum along one axis (\mathbf{x}), along two axes (\mathbf{x}, \mathbf{y}), and along three axes ($\mathbf{x}, \mathbf{y}, \mathbf{z}$).

Table 14: Decay of SuperQuadric occupancy probability: For each neighbourhood value \mathcal{N} , we examine the value of the superquadric occupancy distribution for varying distances.

\mathcal{N}_v	\mathbf{x}	\mathbf{x}, \mathbf{y}	$\mathbf{x}, \mathbf{y}, \mathbf{z}$
1	0.3520	0.3243	0.0959
2	0.2080	0.1769	0.0294
3	0.1114	0.0917	0.0107
4	0.0628	0.0498	0.0042
5	0.0367	0.0280	0.0017
6	0.0220	0.0162	0.0007
7	0.0135	0.0096	0.0003

We observe that for smaller neighbourhood sizes, such as $\mathcal{N} = 3$, the values remain relatively large, meaning superquadrics outside this region cannot be safely ignored. In contrast, for $\mathcal{N} = 5$ there is a substantial reduction in these values, indicating that superquadrics beyond this region have minimal influence. This observation is further supported by the ablation results in Table 5 of the main paper.

B.8 Temporal Flow Module

In Table 15, we train all models without the temporal flow module for comparison. As explained in the main paper, only MLGA is trained without the temporal flow module, as enabling it leads to severe performance degradation due to the rendering proxy being insufficient when rendering across different views.

MLGA achieves the best performance across the main metrics of mIoU and RayIoU, although SQOcc-R performs closely behind. This can be attributed to the approximation technique fitting well when constrained to fixed viewpoints. However, when rendering from multiple views, the supervision signal degrades, making the method less scalable. Additionally, when increasing the superquadric count, MLGA struggles due to limitations in the render proxy.

Table 15: Training models without the temporal flow module: The best result overall is highlighted in **bold**.

Method	IoU	mIoU	RayIoU
GaussianFlowOcc	35.85	11.98	10.38
MLGA	33.67	12.69	10.93
Gaussianization	34.54	12.37	10.22
Voxel NeRF	32.98	11.95	8.07
SQOcc-R	34.70	12.59	10.50

B.9 MLGA versus Single Gaussian Approximation

To evaluate the effectiveness of the MLGA strategy, which uses a multi-layer Gaussian approximation, we compare it with a baseline that approximates each superquadric using a single Gaussian positioned at its centre.

Table 16: MLGA versus a single Gaussian render proxy: The best result overall is highlighted in **bold**.

Approximation	IoU	mIoU
Single Gaussian	31.42	8.74
MLGA	33.67	12.69

The results in Table 16 show that MLGA performs better than a single Gaussian representation, as it more accurately captures the decay of the superquadric occupancy probability. However, as observed in earlier results, this approximation does not provide a sufficiently reliable proxy when rendering from multiple views or when increasing the number of superquadrics.

B.10 Depth Estimation

In Table 17, we re-evaluate our methods for a depth range of $[0.1m, 40m]$, compared to the $[0.1m, 80m]$ range used in the main paper (Table 3b), which was chosen to enable fair comparison with state-of-the-art methods. Here, the range is restricted to $40m$ as this corresponds to the depth perception range of SuperQuadricOcc.

We observe similar trends to those reported in the depth results table in the main paper. SQOcc-R outperforms all methods for Abs Rel, the most important depth metric, which measures absolute relative error. Our method is only slightly outperformed in RMSE by Gaussianisation. MLGA displays noteworthy performance due to the lack of regression to voxel space. Overall, SQOcc-R achieves the best results across all metrics except RMSE.

Table 17: Depth Estimation performance on nuScenes For 40m range.

Method	Abs	Sq	RMSE		δ		
	Rel \downarrow	Rel \downarrow	\downarrow	log \downarrow	$<1.25^\uparrow$	$<1.25^2^\uparrow$	$<1.25^3^\uparrow$
MLGA	0.177	1.144	4.827	0.497	0.753	0.885	0.934
Gaussianization	0.185	1.062	4.365	0.291	0.750	0.888	0.946
Voxel NeRF	0.189	1.171	4.693	0.326	0.722	0.859	0.922
SQOcc-R (Ours)	0.171	0.986	4.444	0.290	0.758	0.894	0.948

B.11 SuperQuadric Parameter Distribution

In Figure 6, we compare the distribution of the superquadric parameters: mean \mathbf{m} , scale \mathbf{s} , epsilon ε , and opacity σ for SQOcc trained with different rendering supervisions: MLGA, Gaussianisation, Voxel NeRF, and SQOcc-R.

Mean \mathbf{m} : For the mean, models trained with the temporal flow module exhibit similar distributions, with superquadrics spread throughout the voxel grid. For MLGA, the xy mean shows superquadrics concentrated closer to the origin, likely due to insufficient supervision in distant regions caused by the absence of temporal flow. For the z mean, a spike around $5m$ appears for models using temporal flow, which may result from the larger region covered by supervision.

Scale \mathbf{s} : For scale, all models show a similar distribution for the xy scale, generally approaching the maximum value of 1 to increase coverage. The z scale shows a slightly broader spread, possibly reflecting the need to model flatter structures such as roads and sidewalks.

Epsilon ε : For epsilon, the average values are approximately $(\varepsilon_1, \varepsilon_2) = (2.0, 0.2)$, corresponding to a diamond-like shape. MLGA and SQOcc-R display slightly more diverse representations, particularly for ε_2 , suggesting that regression to voxel space may produce less varied superquadric shapes.

Opacity σ : For opacity, strong peaks appear at $\sigma = 0$ and $\sigma = 1$, indicating that the models tend to favour near-binary opacity decisions. SQOcc-R and Gaussianisation exhibit similar distributions, while MLGA and Voxel-NeRF show slightly more variation at lower opacity values.

B.12 SuperQuadricOcc Classwise Metrics

In Table 18, we compare the four SQOcc rendering methods in terms of class-wise mIoU for completeness. All models, except MLGA, report relatively similar scores, with SQOcc-R providing the most consistent performance overall, falling only slightly behind the best-performing method for individual classes. For example, for the vulnerable bicycle class, SQOcc-R is only 2% below the top result.

In Table 19, SQOcc-R outperforms all other models in RayIoU across all distance thresholds. For class-wise metrics, it also frequently achieves substantially higher scores than competing methods. For instance, in the bicycle class, SQOcc-R outperforms the next best method by 25%. Overall, SQOcc-R demonstrates superior detection performance.

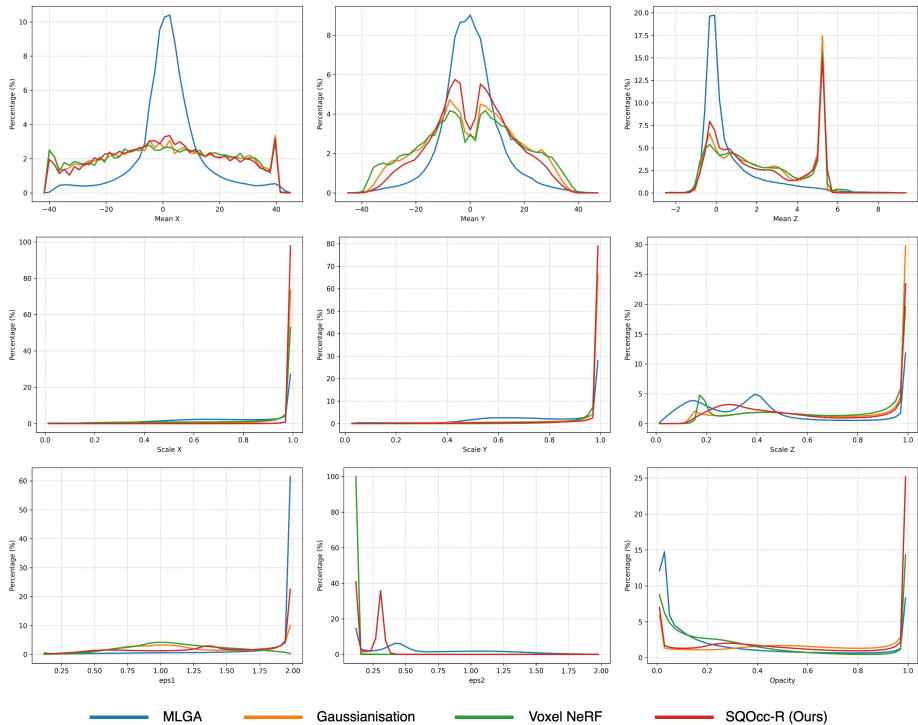


Fig. 6: Parameter comparison for all models: Best viewed zoomed in.

Table 18: SuperQuadricOcc render method mIoU comparison per class on Occ3D-nuScenes [48]: All models are self-supervised. The best-performer is highlighted in bold.

Model			barrier	bicycle	bus	car	const. veh.	motorcycle	pedestrian	traffic cone	trailer	truck	drive. surf.	sidewalk	terrain	manmade	vegetation
	IoU	mIoU															
MLGA	33.67	12.69	5.78	5.69	16.32	13.06	3.72	5.69	3.94	3.54	2.56	11.94	43.58	20.66	24.15	14.45	15.29
Gaussianisation	43.66	16.98	6.01	8.26	13.99	12.59	3.98	9.60	8.70	10.31	1.54	10.26	63.96	32.44	35.89	16.85	20.27
Voxel NeRF	42.94	17.10	7.58	8.53	17.22	14.90	2.02	8.73	7.59	10.47	0.10	12.50	65.67	31.40	34.54	16.26	19.16
SQOcc-R (Ours)	43.51	17.14	6.97	8.34	16.55	14.83	3.42	9.10	8.01	8.77	1.08	12.02	64.71	31.44	34.32	16.56	21.03

Table 19: SuperQuadricOcc render method RayIoU comparison per class on Occ3D-nuScenes [48]: All models are self-supervised. Classwise metrics are taken from RayIoU@2. The best-performer is highlighted in bold.

Model	RayIoU	RayIoU@1	RayIoU@2	RayIoU@4	barrier	bicycle	bus	car	const. veh.	motorcycle	pedestrian	traffic cone	trailer	truck	drive. surf.	sidewalk	terrain	manmade	vegetation
	MLGA	10.93	6.62	10.70	15.49	8.60	6.30	31.90	24.30	4.10	5.70	9.70	4.90	0.80	24.90	18.60	4.20	4.80	14.50
Gaussianisation	14.47	9.37	14.33	19.71	12.40	7.60	26.10	20.30	5.10	7.00	15.50	12.90	0.20	25.00	42.30	12.20	13.30	20.90	22.40
Voxel NeRF	16.56	11.47	16.60	21.62	16.90	7.50	36.00	30.30	2.70	7.50	17.80	16.90	0.00	29.40	46.70	14.70	14.10	21.60	20.20
SQOcc-R (Ours)	17.26	11.92	17.29	22.56	14.90	9.40	38.90	32.00	5.00	8.90	18.80	15.80	0.30	31.80	45.40	13.60	14.10	22.30	22.80

C Supplementary Visualisations

In [subsection C.1](#) we provide additional semantic occupancy and depth estimation visualisations comparing GaussianFlowOcc and SuperQuadricOcc (across our four rendering methods). In [subsection C.2](#) we present visualisation results for SQOcc-R only. Furthermore, we provide a visualisation video comparing SQOcc to the ground truth labels for various scenes attached.

C.1 SuperQuadricOcc Comparisons

In [Figure 7](#), we examine a region in the front-left image of the top scene, which contains several objects, including a vehicle and multiple construction elements. Due to this cluttered environment, many models struggle to reconstruct the vehicle correctly, often producing over-predictions (GaussianFlowOcc, Gaussianisation). In contrast, SQOcc-R reconstructs the vehicle more accurately. It is also important to note that the ground-truth labels for this scene contain inaccuracies, with significant misclassification of certain areas, particularly the road, indicating the need for improvement in labelling pipelines.

In the bottom scene, the view is partially occluded by rain in front of the camera. Despite this, SQOcc-R reconstructs the pole in the back-left image more accurately than the other models. However, all models exhibit some degree of over-prediction, indicating that challenging conditions still lead to degraded performance.

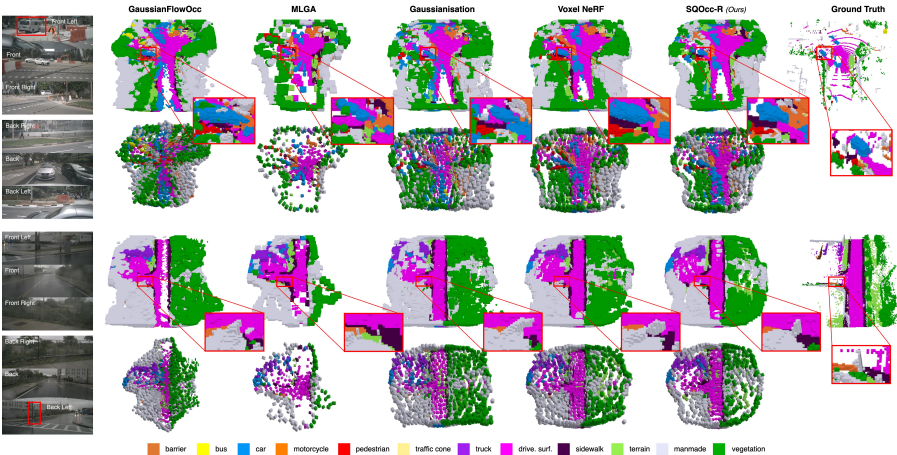


Fig. 7: Semantic Occupancy comparison: Best viewed zoomed in.

In [Figure 8](#), we present a similar analysis for depth estimation. In the front-left image, MLGA and SQOcc-R correctly reconstruct the rigid structure of the trash can, while the other methods produce less precise results. Additionally, the

motorcyclist in the front image is missing in Gaussianisation, whereas MLGA provides the most accurate reconstruction of the shape. In the back-right image, methods that rely on a voxel proxy (Gaussianisation and Voxel NeRF) struggle to reconstruct the thin pole, suggesting that such proxies can lead to fidelity loss, particularly for small or thin objects.

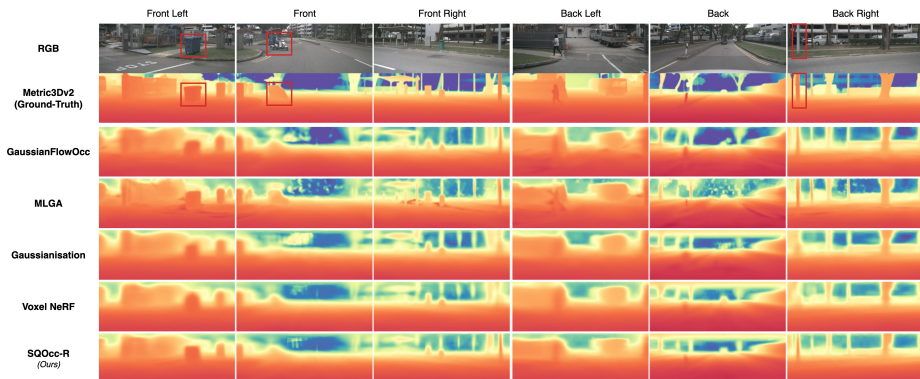


Fig. 8: Dpeth Estimation comparison: Best viewed zoomed in.

C.2 SuperQuadricOcc-Render

For the remaining figures, [Figure 9](#) and [Figure 10](#), we present the semantic occupancy and depth estimation results for SQOcc-R. Our method displays accurate scene reconstruction alongside coherent depth detection.

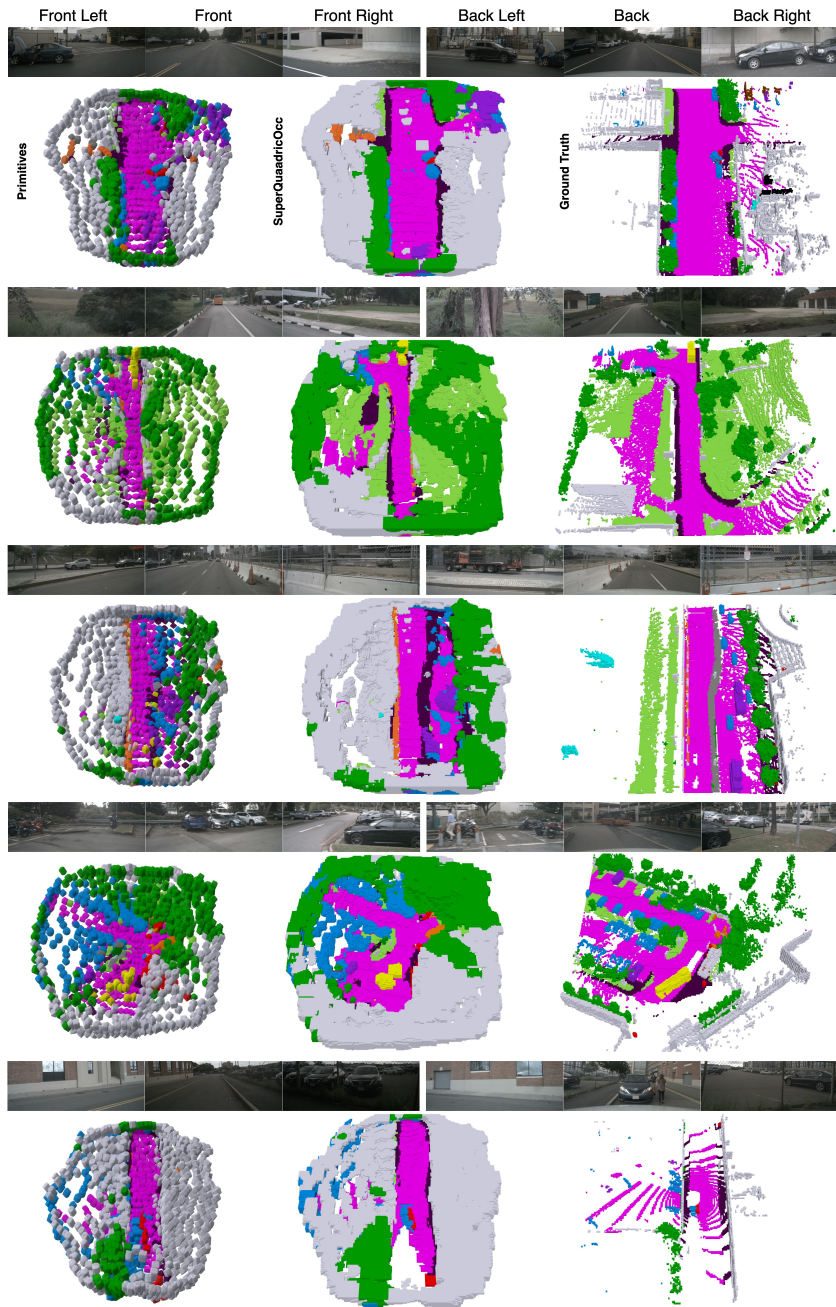


Fig. 9: Semantic Occupancy Estimation for SQOcc-R: We visualise five samples. The left-most images show the superquadric primitives, the centre images show SQOcc-R predictions, and the right images show the ground-truth occupancy labels. Best viewed zoomed in.

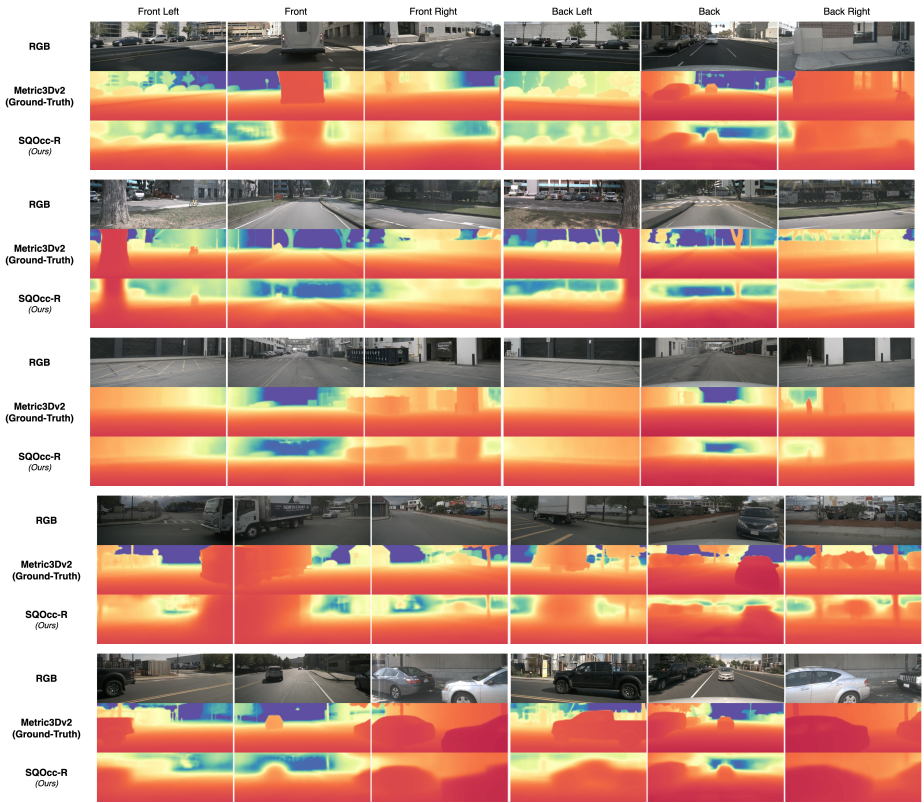


Fig. 10: Depth Estimation for SQOcc-R: Best viewed zoomed in.